

Quarterly Technical Report

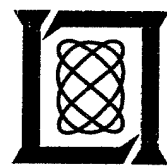
Solid State Research

2000:2

Lincoln Laboratory

MASSACHUSETTS INSTITUTE OF TECHNOLOGY

LEXINGTON, MASSACHUSETTS



Prepared for the Department of the Air Force under Contract F19628-95-C-0002.

Approved for public release; distribution is unlimited.

20001207 011


This report is based on studies performed at Lincoln Laboratory, a center for research operated by Massachusetts Institute of Technology. The work was sponsored by the Department of the Air Force under Contract F19628-95-C-0002.

This report may be reproduced to satisfy needs of U.S. Government agencies.

The ESC Public Affairs Office has reviewed this report, and it is releasable to the National Technical Information Service, where it will be available to the general public, including foreign nationals.

This technical report has been reviewed and is approved for publication.

FOR THE COMMANDER


Gary Tutungian
Administrative Contracting Officer
Plans and Programs Directorate
Contracted Support Management

Non-Lincoln Recipients

PLEASE DO NOT RETURN

Permission is given to destroy this document
when it is no longer needed.

Massachusetts Institute of Technology
Lincoln Laboratory

Solid State Research

Quarterly Technical Report

1 February — 30 April 2000

Issued 22 November 2000

Approved for public release; distribution is unlimited.

ABSTRACT

This report covers in detail the research work of the Solid State Division at Lincoln Laboratory for the period 1 February through 30 April 2000. The topics covered are Quantum Electronics, Electro-optical Materials and Devices, Submicrometer Technology, Biosensor and Molecular Technologies, Advanced Imaging Technology, Analog Device Technology, and Advanced Silicon Technology. Funding is provided by several DoD organizations—including the Air Force, Army, BMDO, DARPA, Navy, NSA, and OSD—and also by the DOE, NASA, and NIST.

TABLE OF CONTENTS

Abstract	iii
List of Illustrations	vii
List of Tables	ix
Introduction	xi
Reports on Solid State Research	xiii
Organization	xxi
1. QUANTUM ELECTRONICS	1
1.1 Temperature Dependence of the Breakdown Voltage for Reverse-Biased GaN p-n-n ⁺ Diodes	1
2. ELECTRO-OPTICAL MATERIALS AND DEVICES	9
2.1 Lattice Misfit Strain Relaxation Determination in Quantum-Dot Heterostructures	9
3. SUBMICROMETER TECHNOLOGY	13
3.1 Interference Lithography at 157 nm	13
3.2 Encapsulated Inorganic Resist Technology	18
4. BIOSENSOR AND MOLECULAR TECHNOLOGIES	23
4.1 Effect of Environmental Contaminants on the Survivability of Engineered B Cells Used in a Bioelectronic Sensor	23
5. ADVANCED IMAGING TECHNOLOGY	27
5.1 Development of Antireflection Coatings for CCD Imagers	27

6.	ANALOG DEVICE TECHNOLOGY	31
6.1	Wideband Photonic Phased-Array Beamformer Design	31
7.	ADVANCED SILICON TECHNOLOGY	35
7.1	MEMS Microswitches	35

LIST OF ILLUSTRATIONS

Figure No.		Page
1-1	Calculated values of the hole concentration p vs donor impurity concentration N_D in compensated GaN with acceptor impurity concentration N_A of $2 \times 10^{19} \text{ cm}^{-3}$ for acceptor binding energy E_A of 200, 300, and 400 mV.	2
1-2	Measured capacitance C (solid curve), and calculated width W (dashed curve) of the depletion region as a function of the applied reverse bias voltage for a 40- μm -diam GaN p-n-n ⁺ diode.	3
1-3	Reverse current vs applied reverse voltage for a 20- μm -diam GaN p-n-n ⁺ diode at $T = 248, 223, 173$, and 123 K.	4
1-4	Breakdown voltage vs temperature of a 20- μm -diam GaN p-n-n ⁺ diode; the open circles denote the data points while the line represents the best fit to the data, using a simple model for the scattering of electrons and holes by phonons.	5
2-1	Cross-sectional centered-dark-field transmission electron micrograph of a heterostructure quantum-dot array. The Moiré patterns, obtained by interference between the quantum-dot and matrix lattice planes, are visible as bright parallel lines within the matrix material.	10
3-1	Optical schematic of the interference lithography system; all components are uncoated. The output of a 157-nm laser enters from the bottom and is split into two arms by the CaF_2 plates. The arms then reflect off Si mirrors and intersect at the sample surface. Alignment of the two beams is achieved by adjusting the angle of the final mirrors.	14
3-2	Scanning electron micrograph of a 50-nm-thick deep-ultraviolet resist (UV6), exposed with the 157-nm interference lithography tool. The period is 94 nm. Note the minimal line edge roughness.	15
3-3	Expanded view of Figure 3-2 showing the same 94-nm period pattern extending over 10 μm^2 . The pattern is visible over the whole exposed area.	15
3-4	Cross-sectional view of patterned resist. These are patterns obtained in the very first exposures with our interference lithography system. The cross-sectional profiles indicate that further system and process optimization is required.	16
3-5	Multiple exposures can create patterns that are more complex than lines and spaces. This image was obtained with two exposures crossed at $\sim 90^\circ$.	16

LIST OF ILLUSTRATIONS (Continued)

Figure No.		Page
3-6	The interference pattern is sensitive to the spatial coherence of the laser. Contrast increases and then decreases again as one arm is translated with respect to the other. Each micrograph represents an additional translation of 18 μm . The results provide an estimate of the spatial coherence length of the F_2 laser.	17
3-7	Comparison of contrast curves of encapsulated inorganic resist technology (EIRT) resists and the commercial resist UV5 with 50-kV electron beam exposure.	19
3-8	Comparison of electron beam imaging of 200- and 300-nm dense and isolated lines of an EIRT resist and the commercial resist UV5.	20
3-9	Comparison of reactive ion etch rates of resists containing increasing amounts of SiO_2 in both an oxygen and chlorine plasma.	20
4-1	Viability of B cells in the presence of contaminants. Dose-response of cells after exposure to (a) urban particulate matter and chimney soot extracts, (b) diesel exhaust extracts for 24 h at 37°C, and (c) saturated solutions (125–250 mg/ml) of soil extracts for 72 h at 28°C.	24
4-2	Undiluted extracts from control, 6-, 11-, and 15-L samples were added to B cells at time zero. Contaminants were removed and replaced with fresh media after 4 and 24 h of exposure at 28°C. Viability was assayed at 72 h from the start of the experiment.	25
5-1	Calculated reflectance vs wavelength for three coatings on a semi-infinite silicon substrate. The HfO_2 film was 48 nm and the SiO_2 80 nm. For the two-layer coating, the TiO_2 was 160 nm and the Al_2O_3 350 nm.	28
5-2	Measured quantum efficiency on back-illuminated CCDs with various coatings. All the data was taken at a device temperature of –50°C with the exception of the $\text{HfO}_2/\text{SiO}_2$ case, which was at room temperature.	28
5-3	Plots of the Fabry-Perot interference effects on three devices in the near infrared using narrowband collimated light.	30
5-4	Peak-peak deviation of the device response due to fringing as a function of wavelength for the three devices of Figure 5-3.	30

LIST OF ILLUSTRATIONS (Continued)

Figure No.		Page
6-1	Schematic view of an rf/photonic phased-array receive antenna. Subarray rf output signals modulate an optical carrier wave (EO converter) and the signals are sent via optical fiber to a photonic true-time-delay (TTD) beamforming network. The combined signal is converted back to rf to provide the beam output.	32
6-2	Schematic diagram showing the basic functionality of a wavelength-multiplexed TTD beamformer. Each of n rf inputs is assigned an optical wavelength and the signals are combined in a wavelength multiplexer. A $1 \times m$ spatial switch selects a fiber Bragg reflective grating that applies the appropriate time delay to each subarray signal. The combined signal is then converted back to rf in the optoelectronic receiver.	33
7-1	Two scanning electron micrograph (SEM) views of single capacitive microswitch. The moving capacitor plate can be seen at the end of the curved cantilever.	36
7-2	SEM photos of the dc contact microswitch open (top) and closed (bottom) states. The corrugations that are added for mechanical stiffness, and the contact dimples can be seen in the cantilever.	37
7-3	Conceptual diagram of two-dimensional microswitch array.	38
7-4	Measurement of capacitive switch characteristics. Each curve is a superposition of the measurement of five devices.	39
7-5	Measurements of dc switch characteristics. Each curve is a superposition of the measurement of three devices.	39

LIST OF TABLES

Table No.		Page
3-1	Comparison of RIE Etch Rates of Resists in Oxygen and Chlorine Plasmas	21

INTRODUCTION

1. QUANTUM ELECTRONICS

Temperature dependence of the breakdown voltage V_B due to impact ionization at high electric fields for reverse-biased GaN p-n-n⁺ diodes has been measured at temperatures T between 98 and 248 K, and the observed increase of V_B with T is in excellent agreement with a simple model for the scattering of carriers by phonons with an effective energy of 42 meV. The impact ionization coefficients for the electrons and holes are nearly equal, and their geometric mean has the value $4 \times 10^4 \text{ cm}^{-1}$ at the breakdown electric fields, in good agreement with recent theoretical results for 300 K.

2. ELECTRO-OPTICAL MATERIALS AND DEVICES

A technique for the measurement of misfit strain relaxation of quantum-dot heterostructures has demonstrated complete misfit strain relaxation in PbSeTe quantum-dot heterostructures within a PbTe matrix. Moiré patterns are obtained using a transmission electron microscopy technique and are quantitatively analyzed to determine the lattice spacing, and hence state of strain, of the quantum-dot material with respect to the unstrained matrix.

3. SUBMICROMETER TECHNOLOGY

A 157-nm interference lithography system capable of patterning features at sub-100-nm pitch has been implemented. Initial results demonstrate ~50-nm line and space patterns exposed in a commercial deep-ultraviolet photoresist with little line edge roughness.

Electron beam imaging, with 200-nm resolution, has been demonstrated using a new encapsulated inorganic resist material. This approach, which combines an inorganic core molecule with a photochemically active layer, is compatible with conventional resist application and development techniques, and it achieves superior plasma etch resistance.

4. BIOSENSOR AND MOLECULAR TECHNOLOGIES

The development of the CANARY (Cellular Analysis and Notification of Antigen Risks and Yields) bioelectronic sensor, which utilizes B cells in a microfluidic chip, has been undertaken to detect and identify pathogens in the environment. As field conditions will expose the sensor to a variety of potentially toxic contaminants, the effect of several of these contaminants on the viability of B cells has been evaluated.

5. ADVANCED IMAGING TECHNOLOGY

Several antireflection coatings have been investigated for use on back-illuminated charge-coupled device imagers, both to improve the quantum efficiency from the visible to the near infrared as well as to reduce Fabry-Perot interference effects in the infrared. A two-layer coating of HfO_2 and SiO_2 has given good results in both respects.

6. ANALOG DEVICE TECHNOLOGY

Photonic beamforming networks for wideband rf phased-array antenna systems have demonstrated significant performance advantages compared to all-rf designs. In addition, they offer reduced size, weight, and power.

7. ADVANCED SILICON TECHNOLOGY

Two novel microelectromechanical systems (MEMS) switch designs have been developed and fabricated in Lincoln Laboratory's Microelectronics Laboratory using silicon CMOS processing techniques. The characteristics of the devices have been measured.

REPORTS ON SOLID STATE RESEARCH

1 FEBRUARY THROUGH 30 APRIL 2000

PUBLICATIONS

- | | | |
|---|---|--|
| Antimonide-Based Mid-Infrared Lasers | H. K. Choi
G. W. Turner | <i>In Long Wavelength Infrared Emitters Based on Quantum Wells and Superlattices</i> , Vol. 6 of <i>Optoelectric Properties of Semiconductors and Superlattices</i> (Gordon and Breach, Newark, N.J., 2000), pp. 225-305 |
| Large-Area Interdigitated Array Microelectrodes for Electro-mechanical Sensing | A. E. Cohen
R. R. Kunz | <i>Sensors Actuators B</i> 62 , 23 (2000) |
| Spectral Beam Combining of a Broad-Stripe Diode Laser Array in an External Cavity | V. Daneu
A. Sanchez
T. Y. Fan
H. K. Choi
G. W. Turner
C. C. Cook | <i>Opt. Lett.</i> 25 , 405 (2000) |
| Temperature Dependence of Spin-Lattice Relaxation in Rare-Earth Iron Garnets | G. F. Dionne
G. L. Fitch | <i>J. Appl. Phys.</i> 87 , 4963 (2000) |
| A Comparison of DNQ/Novolac Resists for E-Beam Exposure | T. H. Fedynyshyn
S. P. Doran
M. L. Lind
T. M. Lyszczarz
W. F. DiNatale
D. Lennon
C. Sauer
J. Meute | <i>Proc. SPIE</i> 3873 , 600 (1999) |

Chemical Concentrator for Rapid Vapor Detection	M. W. Geis R. R. Kunz	<i>Proc. SPIE</i> 3710 , 421 (1999)
Photo-Induced Organic Contamination of Lithographic Optics	R. R. Kunz V. Liberman D. K. Downs	<i>Microlithogr. World</i> 9 , 2 (2000)
Proton Bombardment for Enhanced Four-Wave Mixing in InGaAsP-InP Waveguides	E. R. Thoen J. P. Donnelly S. H. Groves K. L. Hall E. P. Ippen	<i>IEEE Photon. Technol. Lett.</i> 12 , 311 (2000)
High-Brightness Tapered Laser Sources in the 1.3- to 2.0- μm Wavelength Range	J. N. Walpole J. P. Donnelly H. K. Choi Z. L. Liao L. J. Missaggia R. J. Bailey S. H. Groves G. W. Turner P. J. Taylor V. Daneu	<i>Proc. SPIE</i> 3947 , 40 (2000)
Gaussian Patterned Contacts for Improved Beam Stability of 1.55 μm Tapered Lasers	J. N. Walpole J. P. Donnelly L. J. Missaggia Z. L. Liao S. R. Chinn S. H. Groves P. J. Taylor	<i>IEEE Photon. Technol Lett.</i> 12 , 257 (2000)
Correlation Between Surface Step Structure and Phase Separation in Epitaxial GaInAsSb	C. A. Wang	<i>Appl. Phys. Lett.</i> 76 , 2077 (2000)

ACCEPTED FOR PUBLICATION

Multiport-Readout Frame-Transfer
5 Megapixel CCD Imaging System
for TEM Applications

B. E. Burke

Ultramicroscopy

All-Active InGaAsP/InP Optical
Tapered-Amplifier $1 \times N$ Power
Splitters

J. P. Donnelly

IEEE Photon. Technol. Lett.

R. E. Reeder

R. J. Bailey

P. J. Taylor

A. Napoleone

W. D. Goodhue

S. S. Choi*

Experimentation and Modeling of
Organic Photocontamination on
Lithographic Optics

R. R. Kunz

J. Vac. Sci. Technol. B

V. Liberman

D. K. Downs

Spectroscopy of Competing
Mechanisms Generating
Stimulated Emission in GaN

R. Molnar

Appl. Phys. Lett.

W. D. Herzog*

G. E. Bunea*

M. S. Ünlü*

B. B. Goldberg*

PRESENTATIONS[†]

Sub-0.25 μm Fully Depleted
Silicon-on-Insulator Technology

R. P. D'Onofrio

Deep-Space One Technology

C. L. Keast

Validation Symposium,

P. W. Wyatt

Pasadena, California,

A. M. Soares

8-9 February 2000

*Author not at Lincoln Laboratory.

[†] Titles of presentations are listed for information only. No copies are available for distribution.

Diode-Pumped 214.8-nm Nd:YAG/
Cr⁴⁺:YAG Microchip Laser
System for the Detection of NO

J. Wormhoudt*
J. H. Shorter*
J. J. Zayhowski

Laser Applications to
Chemical and Environmental
Analysis Meeting,
Santa Fe, New Mexico,
11-14 February 2000

Passively *Q*-Switched 214.8-nm
Nd:YAG/Cr⁴⁺:YAG Microchip
Laser System for the Detection of
NO

J. J. Zayhowski
C. C. Cook
J. Wormhoudt*
J. Shorter*

Advanced Solid State Lasers
Topical Meeting,
Davos, Switzerland,
13-16 February 2000

Miniature Sources of
Subnanosecond 1.4–4.3- μ m Pulses
with High Peak Power

J. J. Zayhowski
A. L. Wilson

Advanced Solid State Lasers
Topical Meeting,
Davos, Switzerland,
13-16 February 2000

Optical Sampling for Analog to
Digital Conversion

P. W. Juodawlkis
J. C. Twichell
R. C. Williamson

IEEE Electron Devices Society
Meeting,
MIT Lincoln Laboratory,
Lexington, Massachusetts,
23 February 2000

High-Brightness Tapered Laser
Sources Emitting in the 1.3- to
2.0- μ m Wavelength Range

J. N. Walpole

Lincoln Laboratory
Technical Seminar Series,
University of Massachusetts,
Amherst, Massachusetts,
23 February 2000

Laser Cleaning of Optical Elements
in 157-nm Lithography

T. M. Bloomstein
M. Rothschild
V. Liberman
D. E. Hardy
N. N. Efremow, Jr.
S. T. Palmacci

SPIE Microlithography
Symposium 2000,
Santa Clara, California,
27 February–3 March 2000

*Author not at Lincoln Laboratory.

Encapsulated Inorganic Resist
Technology

T. H. Fedynyshyn
S. P. Doran
M. L. Lind
E. Matijevich*
I. Sonji*

SPIE Microlithography
Symposium 2000,
Santa Clara, California,
27 February–3 March 2000

Prospects for Using Existing
Resists for Evaluating 157-nm
Imaging Systems

T. H. Fedynyshyn
R. R. Kunz
S. P. Doran
R. B. Goodman
M. L. Lind
J. E. Curtin

SPIE Microlithography
Symposium 2000,
Santa Clara, California,
27 February–3 March 2000

Application of Chromeless Phase-
Shift Masks to Sub-100 nm SOI
CMOS Transistor Fabrication

M. Fritze
J. M. Burns
P. W. Wyatt
D. K. Astolfi
T. Forte
D. Yost
P. Davis
A. Curtis
D. M. Preble
S. Cann
S. Deneault
H. Y. Liu*
J. C. Shaw*
N. T. Sullivan*
R. Brandom*
M. Mastovich*

SPIE Microlithography
Symposium 2000,
Santa Clara, California,
27 February–3 March 2000

*Author not at Lincoln Laboratory.

Application of Attenuated Phase-Shift Masks to Sub-0.18 μm Logic Patterns

M. Fritze
P. W. Wyatt
D. K. Astolfi
P. V. Davis
A. Curtis
D. M. Preble
S. G. Cann
S. J. Deneault
D. Chan*
J. Shaw*
N. Sullivan*
R. Brandom*
M. Mastovich*

SPIE Microlithography Symposium 2000,
Santa Clara, California,
27 February–3 March 2000

New Materials for 157-nm Photoresists: Characterization and Properties

R. R. Kunz
M. K. Crawford*
E. Feiring*
J. Feldman*
R. French*
M. Periysamy*
F. L. Schadt*
R. J. Smalley*
F. C. Zumsteg*
V. Rao*
S. M. Holl*

SPIE Microlithography Symposium 2000,
Santa Clara, California,
27 February–3 March 2000

Experimentation and Modeling of Organic Photocontamination on Lithographic Optics

R. R. Kunz
V. Liberman
D. K. Downs

SPIE Microlithography Symposium 2000,
Santa Clara, California,
27 February–3 March 2000

Determination of Optical Properties of Thin Films and Surfaces in 157-nm Lithography

V. Liberman
T. M. Bloomstein
M. Rothschild

SPIE Microlithography Symposium 2000,
Santa Clara, California,
27 February–3 March 2000

*Author not at Lincoln Laboratory.

Long-Term Testing of Optical Components for 157-nm Lithography	V. Liberman M. Rothschild J. H. C. Sedlacek R. S. Uttaro A. K. Bates* K. Orvek*	SPIE Microlithography Symposium 2000, Santa Clara, California, 27 February–3 March 2000
Interference Lithography at 157 nm	M. Switkes T. M. Bloomstein M. Rothschild	SPIE Microlithography Symposium 2000, Santa Clara, California, 27 February–3 March 2000
$\text{Al}_x\text{Ga}_{1-x}\text{N}$ Avalanche Photodiodes	K. A. McIntosh R. J. Molnar S. Verghese J. C. Twichell	2000 DARPA/MTO Solar Blind Detector Review, Westlake Village, California, 29 February–1 March 2000
HVPE-Grown GaN Avalanche Photodiodes	R. J. Molnar S. Verghese K. A. McIntosh L. J. Mahoney K. M. Molvar R. L. Aggarwal I. Melngailis	6th Wide Bandgap III-Nitride Workshop, Richmond, Virginia, 12-15 March 2000
Laser Beam Combining for Power and Brightness Scaling	T. Y. Fan A. Sanchez V. Daneu R. L. Aggarwal S. C. Buchter A. Goyal C. C. Cook	IEEE Aerospace Conference, Big Sky, Montana, 18-25 March 2000
PbTe/PbSeTe Quantum-Dot Superlattices with High Thermoelectric Figures of Merit	T. C. Harman	American Physical Society Meeting, Minneapolis, Minnesota, 20-24 March 2000

*Author not at Lincoln Laboratory.

Extending the Performance of
Optically Sampled Analog-to-Digi-
tal Converters

P. W. Juodawlkis
J. L. Wasserman
G. E. Betts
R. C. Williamson
J. C. Twichell

DARPA/MTO PACT Review,
San Diego, California,
22-23 March 2000

HVPE-Grown GaN Avalanche
Photodiodes

S. Verghese
K. A. McIntosh
R. J. Molnar
L. J. Mahoney
K. Molvar
R. L. Aggarwal
I. Melngailis

Doping, Dopants, and Carrier
Dynamics in Wide Gap
Semiconductors Workshop,
Copper Mountain, Colorado,
2-6 April 2000

Fast Vapor Concentrator

M. W. Geis
R. R. Kunz

Meeting of the New England
Chapter, American Vacuum
Society,
Burlington, Massachusetts,
24 April 2000

High Thermoelectric Figures of
Merit in PbTe/PbSnSeTe Quantum
Dot Superlattices

T. C. Harman
P. J. Taylor
D. L. Spears
M. P. Walsh

2000 Materials Research
Society Meeting,
San Francisco, California,
24-28 April 2000

BAWS Principle of Operation

T. H. Jeys

Industry Day Briefing for
Bio-Aerosol Warning System,
MIT Lincoln Laboratory,
Lexington, Massachusetts,
27 April 2000

Overview of GaSb-Based Materials
at MIT Lincoln Laboratory

G. W. Turner

Lincoln Laboratory
Technical Seminar Series,
University of Southern
California,
Los Angeles, California,
28 April 2000

ORGANIZATION

SOLID STATE DIVISION

D. C. Shaver, *Head*
R. W. Ralston, *Associate Head*
N. L. DeMeo, Jr., *Assistant*
Z. J. Lemnios, *Senior Staff*

J. W. Caunt, *Assistant Staff*
K. J. Challberg, *Administrative Staff*
J. D. Pendergast, *Administrative Staff*

SUBMICROMETER TECHNOLOGY

M. Rothschild, *Leader*
T. M. Lyszczarz, *Assistant Leader*
T. H. Fedynyshyn, *Senior Staff*
R. R. Kunz, *Senior Staff*

Astolfi, D. K.
Bloomstein, T. M.
DiNatale, W. F.
Doran, S. P.
Efremow, N. N., Jr.
Forte, A. R.
Geis, M. W.
Goodman, R. B.
Krohn, K. E.

Liberman, V.
Maki, P. A.
Palmacci, S. T.
Sedlacek, J. H. C.
Spector, S. J.
Switkes, M.
Sworin, M.
Uttaro, R. S.

QUANTUM ELECTRONICS

A. Sanchez-Rubio, *Leader*
T. Y. Fan, *Assistant Leader*
T. H. Jeys, *Senior Staff*
J. J. Zayhowski, *Senior Staff*

Aggarwal, R. L.
Buchter, S. C.
Daneu, J. L.
Daneu, V.

DiCecca, S.
Goyal, A. K.
O'Brien, P. W.
Ochoa, J. R.

ELECTRO-OPTICAL MATERIALS AND DEVICES

J. C. Twichell, *Leader*
D. L. Spears, *Assistant Leader**
G. W. Turner, *Assistant Leader*
H. K. Choi, *Senior Staff*
R. C. Williamson, *Senior Staff*

Bailey, R. J.
Betts, G. E.
Calawa, A. R.*
Calawa, D. R.
Calawa, S. D.
Connors, M. K.
Donnelly, J. P.
Goodhue, W. D.
Hargreaves, J. J.
Harman, T. C.

Harris, C. T.
Juodawilkis, P. W.
Liau, Z. L.
Mahoney, L. J.
Manfra, M. J.
McIntosh, K. A.
Missaggia, L. J.
Molnar, R. J.
Mull, D. E.
Napoleone, A.

Nitishin, P. M.
Oakley, D. C.
O'Donnell, F. J.
Poillucci, R. J.
Taylor, P. J.
Verghese, S.
Walpole, J. N.
Wang, C. A.
Wasserman, J. L.

*Part Time

BIOSENSOR AND MOLECULAR
TECHNOLOGIES

M. A. Hollis, *Leader*

Blanchard, D. J.	Parameswaran, L.
Graves, C. A.	Petrovick, M. S.
Harper, J. D.	Rider, T. H.
Mathews, R. H.	Young, A. M.
Nargi, F. E.	

ANALOG DEVICE TECHNOLOGY

T. C. L. G. Sollner, *Leader*
L. M. Johnson, *Assistant Leader*
A. C. Anderson, *Senior Staff*

Anthony, M. P.	Murphy, P. G.
Berggren, K. K.	Oates, D. E.
Boisvert, R. R.	Sage, J. P.
Feld, D. A.	Santiago, D. D.
Fitch, G. L.	Seaver, M. M.
Holtham, J. H.	Slattery, R. L.
Lyons, W. G.	Weir, T. J.
Macedo, E. M., Jr.	Whittington, R. H.

ADVANCED IMAGING TECHNOLOGY

B. B. Kosicki, *Leader*
R. K. Reich, *Assistant Leader*
B. E. Burke, *Senior Staff*

Aull, B. F.	Johnson, K. F.
Cooper, M. J.	Lind, T. A.
Craig, D. M.	Loomis, A. H.
Daniels, P. J.	McGonagle, W. H.
Doherty, C. L., Jr.	O'Mara, D. M.
Dolat, V. S.	Percival, K. A.
Felton, B. J.	Rathman, D. D.
Gregory, J. A.	Young, D. J.

ADVANCED SILICON TECHNOLOGY

C. L. Keast, *Leader*
P. W. Wyatt, *Associate Leader*

Austin, E. E.	Newcomb, K. L.
Berger, R.	Rabe, S.
Bozler, C. O.	Reinold, J. H., Jr.
Burns, J. A.	Soares, A. M.
Chen, C. K.	Suntharalingam, V.
Chen, C. L.	Travis, L.
Davis, P. V.	Tyrrell, B. M.
D'Onofrio, R. P.	Warner, K.
Fritze, M.	Yost, D.-R.
Gouker, P. M.	Young, G. R.
Knecht, J. M.	

1. QUANTUM ELECTRONICS

1.1 TEMPERATURE DEPENDENCE OF THE BREAKDOWN VOLTAGE FOR REVERSE-BIASED GaN p-n-n⁺ DIODES

Gallium-aluminum nitride (Ga_{1-x}Al_xN) photodiodes are being developed for solar-blind uv applications [1]–[4]. There are also reports of avalanche photodiodes (APDs) that operate in the linear mode with gains between 10 and 20 [5],[6]. We have recently developed a GaN p-n-n⁺ APD that has been successfully used in the Geiger mode for the detection of single uv photons [7]. Here, we report on the temperature dependence of the avalanche breakdown voltage V_B for a reverse-biased p-n-n⁺ diode at temperatures between 98 and 248 K. The observed temperature dependence of V_B is found to be in excellent agreement with a simple model for the scattering of electrons and holes by phonons. Previously, avalanche breakdown was reported for GaN p- π -n diodes [8] and GaN p-n diodes [9] in the temperature range from 300 to 600 K. However, the temperature dependence of the breakdown voltage in both of these cases was smaller than that expected from the phonon scattering model. Before presenting the results for the breakdown, we discuss the effect of donor impurity compensation on the hole concentration in the p layer. We also present the results of the capacitance-voltage (C-V) measurements, which yield information on the width of the depletion region as well as on the concentrations of donor impurities in the n and n^+ regions.

The p , n , and n^+ layers of the diode structure were deposited on a $\sim 7\text{-}\mu\text{m}$ -thick unintentionally n -type ($<10^{17}\text{ cm}^{-3}$) GaN film on a sapphire substrate, using hydride vapor phase epitaxy (HVPE) [10], where GaCl, obtained by passing HCl over metallic Ga, is reacted with NH_3 to form GaN. The entire film, including the diode structure, was produced by HVPE in an uninterrupted growth cycle on a sapphire substrate prepared with a ZnO pretreatment. The n^+ layer was doped with Si to a density of $\sim 4 \times 10^{18}\text{ cm}^{-3}$ and had a thickness of $\sim 0.5\text{ }\mu\text{m}$. The n layer was unintentionally n -type ($<10^{17}\text{ cm}^{-3}$) and had a thickness of $\sim 0.25\text{ }\mu\text{m}$. The p layer was doped with Zn to a density of $\sim 2 \times 10^{19}\text{ cm}^{-3}$ and had a thickness of $\sim 0.25\text{ }\mu\text{m}$. Even though the p layer is heavily doped with Zn, it has a relatively low hole concentration. This may be understood by considering the relatively large value of the binding energy E_A for Zn acceptors and the effect of compensation due to the presence of background donor impurities.

In compensated p -type semiconductors, the hole concentration p is given by [11]

$$p(p + N_D)/(N_A - N_D - p) = \left(2\pi m_d k_B T / h^2\right)^{3/2} \exp(-E_A/k_B T) \quad (1.1)$$

where N_D is the donor impurity concentration, N_A is the acceptor impurity concentration, m_d is the hole density-of-states effective mass, k_B is the Boltzmann constant, T is the temperature, and h is the Planck's constant. Using Equation (1.1), we have calculated p as a function of N_D up to $2 \times 10^{18}\text{ cm}^{-3}$, taking m_d as equal to the free electron mass m_0 , and $N_A = 2 \times 10^{19}\text{ cm}^{-3}$. The calculated values of p are plotted in Figure 1-1 for three different values of E_A equal to 200, 300, and 400 meV.

The binding energy of the Mg and Zn acceptors in GaN has been deduced to be 224 and 400 meV, respectively, from the energy of the photoluminescence peaks arising from free excitons and acceptor-bound excitons [12]. If all the Zn atoms are assumed to be available for thermal excitation of holes, the p vs N_d curve for $E_A = 400$ meV in Figure 1-1 would imply a value of $p \sim 5 \times 10^{15} \text{ cm}^{-3}$ for uncompensated ($N_D = 0$) material. However, we expect $N_D \sim 1 \times 10^{17} \text{ cm}^{-3}$, based on the carrier concentration in the unintentionally n -type material. For this value of N_D , p is $\sim 3 \times 10^{14} \text{ cm}^{-3}$, which is more than an order-of-magnitude smaller than the corresponding value for the uncompensated material.

Diodes used in this work were fabricated as in [5] with the exception that the semitransparent window was replaced with an opaque 55-nm Ti/340-nm Au film. Electrical contact with the p layer was made by attaching a gold wire to this Ti/Au film. Electrical contact with the n layer was made with an indium dot that was soldered to a nearby region from which both the oxide and the p layers had been removed.

We made C-V measurements on one of the diodes with a diameter of 40 μm , using a Hewlett-Packard CV meter model 4284, which allows the application of reverse bias up to 40 V. The low

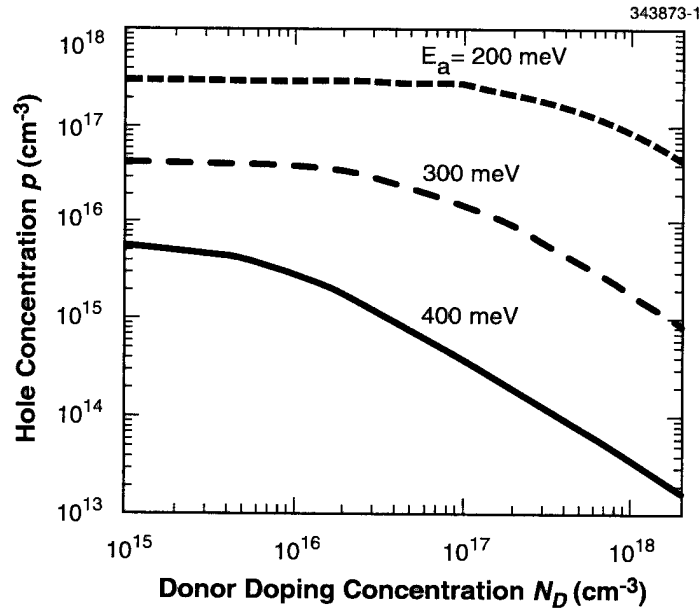


Figure 1-1. Calculated values of the hole concentration p vs donor impurity concentration N_D in compensated GaN with acceptor impurity concentration N_A of $2 \times 10^{19} \text{ cm}^{-3}$ for acceptor binding energy E_A of 200, 300, and 400 mV.

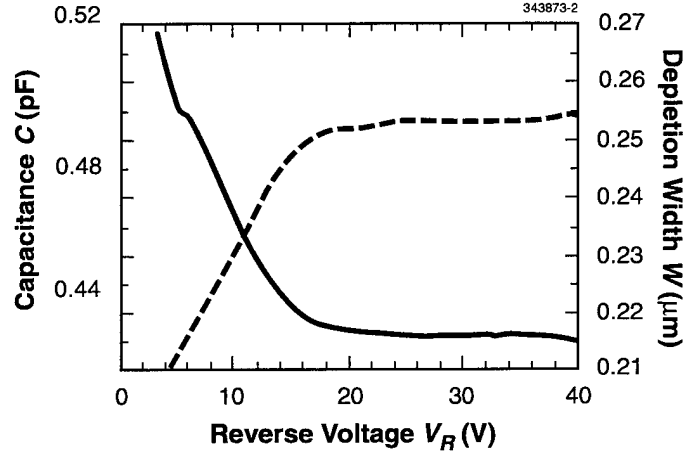


Figure 1-2. Measured capacitance C (solid curve), and calculated width W (dashed curve) of the depletion region as a function of the applied reverse bias voltage for a 40- μm -diam GaN $p\text{-}n\text{-}n^+$ diode.

capacitance (<1 pF) of the GaN diodes and the presence of relatively high noise in the measurement laboratory required filters and a Faraday cage around the probing station for reliable C-V measurements. The measurements were made at a frequency of 1.0 MHz. Figure 1-2 shows the measured capacitance C as a function of the applied reverse voltage V_R .

The capacitance of a diode is given by

$$C = \epsilon_0 \epsilon A / W \quad (1.2)$$

where $\epsilon_0 = 8.854 \times 10^{-12}$ F/m is the electric permittivity of the vacuum, ϵ is the dielectric constant of GaN, A is the area of the diode, and W is the width of the depletion region. Using a value of $\epsilon = 9.6$ for GaN, $A = 1.26 \times 10^{-9}$ m², and the measured values of C in Equation (1.2), we have calculated values of W as a function of V_R . A plot of W vs V_R is included in Figure 1-2.

The derivative of $1/C^2$ with respect to V_R is given by

$$d(1/C^2)/dV_R = 2/(eA^2 \epsilon_0 \epsilon N) \quad (1.3)$$

with

$$N = (N_D^+ N_A^-) / (N_D^+ + N_A^-) \quad (1.4)$$

where e is the magnitude of the electronic charge, N_D^+ is the concentration of the ionized donors in the depleted n or n^+ layer, and N_A^- is the concentration of the ionized acceptors in the depleted p layer. Assuming that $N_A^- \gg N_D^+$, N is approximately equal to N_D^+ . Thus, a determination of N as a function of V_R , using the C-V data, yields values of 8×10^{16} and $2 \times 10^{18} \text{ cm}^{-3}$ for the donor impurity concentrations in the n and n^+ layers, respectively. These values of N and W are consistent with those determined from secondary ion mass spectroscopy (SIMS) data for a piece of the same wafer.

The current-voltage measurements were made on a $20\text{-}\mu\text{m}$ -diam diode placed on the cold finger of a Joule-Thomson refrigerator [13], using a Hewlett-Packard semiconductor parameter analyzer, model 4145 A. Figure 1-3 shows the measured reverse current plotted against V_R for $T = 248, 223, 173$, and 123 K . The abrupt increase in the current at high values of V_R indicates the onset of avalanche breakdown. Note the monotonic increase in the breakdown voltage with temperature.

The variation of the breakdown voltage with temperature can be understood in terms of a simple model for the scattering of electrons and holes by phonons as follows. The energy gained by a charge carrier accelerated in an electric field is proportional to its mean free path λ and the magnitude of the applied electric field. The energy gain necessary for impact ionization must be at least equal to the energy gap E_g . Assuming that λ is limited by phonon scattering, the variation of λ with temperature is given by [14]

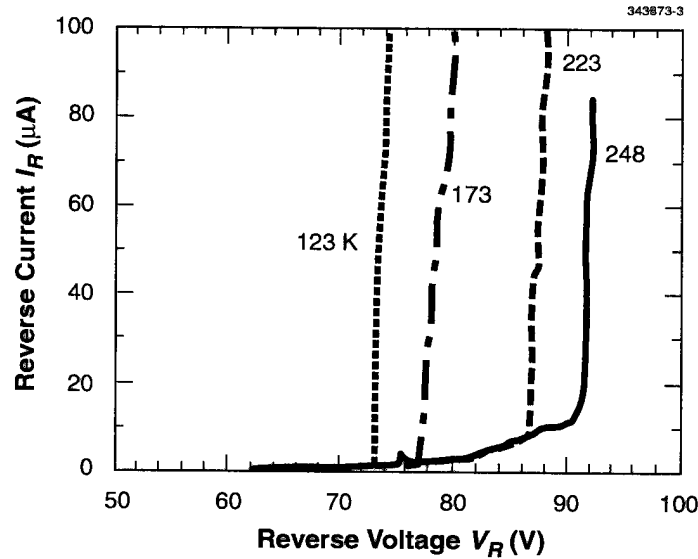


Figure 1-3. Reverse current vs applied reverse voltage for a $20\text{-}\mu\text{m}$ -diam GaN $p\text{-}n\text{-}n^+$ diode at $T = 248, 223, 173$, and 123 K .

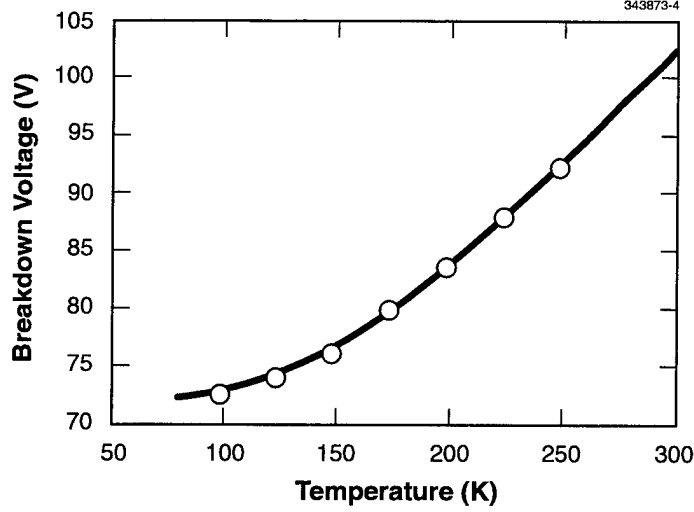


Figure 1-4. Breakdown voltage vs temperature of a 20- μm -diam GaN $p\text{-}n\text{-}n^+$ diode; the open circles denote the data points while the line represents the best fit to the data, using a simple model for the scattering of electrons and holes by phonons.

$$\lambda = \lambda_0(2N+1)^{-1} \quad (1.5)$$

where λ_0 is the mean free path at $T = 0$ K, and N is the phonon occupation number given by

$$N = \left[\exp(h\nu_q/k_B T) - 1 \right]^{-1} \quad (1.6)$$

where $h\nu_q$ represents the effective energy of the phonons involved in the scattering process. Hence, the breakdown voltage is given by

$$V_B = [E_g W / e\lambda_0](2N+1) \quad (1.7)$$

Using Equation (1.7) and the values $E_g(300 \text{ K}) = 3.4 \text{ eV}$, $dE_g/dT = 0.67 \text{ meV/K}$ [15], $\lambda_0 = 13 \text{ nm}$, and $h\nu_q = 42.3 \text{ meV}$, we have fit the model to the data, as shown in Figure 1-4. Clearly, there is a good fit of the data to the model. The 13-nm value for λ_0 is typical of the values observed in semiconductors. The 42.3-meV value for the effective phonon energy is in the range of the energies of the Raman-active phonons [16]: 17.8 [E_2], 65.8 [A_1 (TO)], 69.3 [E_1 (TO)], 70.3 [E_2], 87.7 [A_1 (LO)], and 91.7 [E_1 (LO)] meV.

For $T \geq 200 \text{ K}$, the predicted increase of V_B with temperature is approximately linear with $dV_B/dT \sim 0.2 \text{ V/K}$, compared with the much smaller values of 0.02 and 0.004 V/K in [8] and [9], respectively. The lower values of V_B/dT , as obtained in the previous work, may be related to the presence of defects responsible for the observation of microplasmas.

Assuming that the electric field in the depletion region is uniform, the avalanche breakdown condition, as obtained from Equation 28 in [17], is given by

$$(\alpha_B - \beta_B)/(\ln \alpha - \ln \beta) = 1/W \quad (1.8)$$

where α_B and β_B are the impact ionization coefficients at breakdown for the electrons and holes, respectively. When α_B and β_B are of the same order of magnitude, the breakdown condition may be written in a simpler form as

$$(\alpha_B \beta_B)^{1/2} = 1/W \quad (1.9)$$

which implies that the effective value of the impact ionization coefficient at breakdown is equal to the geometric mean of α_B and β_B . Equation (1.9) is attractive from the point of view of physical intuition. Substituting $W = 0.26 \mu\text{m}$ in Equation (1.9), we obtain $(\alpha_B \beta_B)^{1/2} = 4 \times 10^4 \text{ cm}^{-1}$, independent of the temperature. From the curve in Figure 1-4, the breakdown voltage at 300 K is 103 V, corresponding to an electric field of 4 MV/cm. For this value of the electric field, the theoretical values [18] of α and β are 5×10^4 and $4 \times 10^4 \text{ cm}^{-1}$, which are in good agreement with our deduced value of $4 \times 10^4 \text{ cm}^{-1}$ for $(\alpha_B \beta_B)^{1/2}$.

The results presented here have an important implication regarding the performance of GaN APDs. The fact that the electron and hole multiplication rates are nearly equal implies the presence of excess noise for continuous operation. However, this excess noise may not be important in the case of the Geiger-mode operation for the detection of single photons.

R. L. Aggarwal	R. J. Molnar
I. Melngailis	M. W. Geis
S. Verghese	L. J. Mahoney

REFERENCES

1. D. Walker, V. Kumar, K. Mi, P. Sandvik, P. Kung, X. H. Zhang, and M. Razeghi, *Appl. Phys. Lett.* **76**, 403 (2000).
2. G. Y. Xu, A. Salvador, W. Kim, Z. Fan, C. Lu, H. Tang, H. Morkoç, G. Smith, M. Estes, B. Goldenberg, W. Yang, and S. Krishnakutty, *Appl. Phys. Lett.* **71**, 2154 (1997).
3. A. Osinsky, S. Gangopadhyay, R. Gaska, B. Williams, M. A. Khan, D. Kubsenkov, and H. Temkin, *Appl. Phys. Lett.* **71**, 2334 (1997).
4. J. M. Van Hove, R. Hickman, J. J. Klaassen, P. P. Chow, and P. P. Rudden, *Appl. Phys. Lett.* **70**, 2282 (1997).
5. K. A. McIntosh, R. J. Molnar, L. J. Mahoney, A. Lightfoot, M. W. Geis, K. M. Molvar, I. Melngailis, R. L. Aggarwal, W. D. Goodhue, S. S. Choi, D. L. Spears, and S. Verghese, *Appl. Phys. Lett.* **75**, 3485 (1999).

6. J. C. Carrano, D. J. H. Lambert, C. J. Eiting, C. J. Collins, T. Li, S. Wang, B. Yang, A. L. Beck, R. D. Dupuis, and J. C. Campbell, *Appl. Phys. Lett.* **76**, 924 (2000).
7. K. A. McIntosh, R. J. Molnar, L. J. Mahoney, K. M. Molvar, N. Efremow, Jr., and S. Verghese, *Appl. Phys. Lett.* **76**, 3938 (2000).
8. A. Osinsky, M. S. Shur, R. Gaska, and Q. Chen, *Electron. Lett.* **34**, 691 (1998).
9. V. A. Dimitriev, K. G. Irvine, C. H. Carter, Jr., N. I. Kuznestov, and E. V. Kalinina, *Appl. Phys. Lett.* **68**, 229 (1996).
10. R. J. Molnar, W. Götz, L. T. Romano, and N. M. Johnson, *J. Cryst. Growth* **178**, 147 (1997).
11. See, for example, K. Seeger, *Semiconductor Physics* (Springer-Verlag, New York, 1982), p. 42.
12. B. J. Skromme and G. L. Martinez, presented at the 1999 Fall Meeting of the Materials Research Society, Boston, Mass., 29 Nov.–3 Dec. 1999.
13. Model K2205, MMR Technologies, Inc., Mountain View, Calif.
14. See, for example, F. Capasso, in *Semiconductors and Semimetals*, R. K. Willardson and A. C. Beer, eds. (Academic, New York, 1985), Vol. 22, Pt. D, p. 36.
15. D. L. Camphausen and G. A. N. Connell, *J. Appl. Phys.* **42**, 4438 (1971).
16. See, for example, *Properties of Group III Nitrides* (INSPEC, Institution of Electrical Engineers, London, 1994), p. 252.
17. G. E. Stillman and C. M. Wolfe, in *Semiconductors and Semimetals*, R. K. Willardson and A. C. Beer, eds. (Academic, New York, 1977), Vol. 12, p. 303.
18. I. H. Oguzman, E. Bellotti, K. F. Brennan, J. Kolnik, R. Wang, and P. P. Ruden, *J. Appl. Phys.* **81**, 7827 (1997).

2. ELECTRO-OPTICAL MATERIALS AND DEVICES

2.1 LATTICE MISFIT STRAIN RELAXATION DETERMINATION IN QUANTUM-DOT HETEROSTRUCTURES

The incorporation of low-dimensional quantum-dot heterostructures can impart novel and unique properties to a material [1]. There are many techniques that can be used to obtain quantum-dot heterostructures; one of the most common is the Stranski-Krastinow (S-K) growth mode. This growth mode is characterized by formation of nanometer-size islands having a hemispherical cap shape from an initially flat, highly lattice misfit strained monolithic film. The S-K technique has an important limitation in that there is typically little control of the physical properties of the obtained quantum-dot heterostructures, such as the distribution of island size and the state of misfit strain relaxation of the islands.

Because quantum-dot heterostructures are typically not uniform, less conventional techniques will be required for characterizing their relevant physical properties. Here, we describe a Moiré pattern analysis using transmission electron microscopy (TEM) to characterize the state of lattice misfit strain relaxation in quantum-dot heterostructures.

Moiré patterns arise from the interference between two highly periodic structures. For the present TEM analysis, the periodic structures are the lattice planes of the matrix and quantum-dot materials. The Moiré patterns can be analyzed to determine the lattice spacings, and changes in lattice spacings, of the quantum dot material and the matrix material, and therefore a measure of the lattice strain is obtained. For quantum-dot heterostructures, there can be rotational Moiré patterns where the lattice planes of the matrix and the quantum dot are rotated with respect to each other by an angle α , parallel Moiré patterns where the spacing of the lattice planes of the quantum-dot d_1 and matrix d_2 are naturally different, or a combination of the two. The spacing of the Moiré pattern D having both rotational and parallel character is given by the following relation [2]:

$$D = d_1 d_2 / (d_1^2 + d_2^2 - 2d_1 d_2 \cos \alpha)^{0.5} \quad (2.1)$$

Shown in Figure 2-1 is a centered-dark-field image of an array of quantum dots whose composition is essentially PbSe within a matrix of PbTe. The inset shows the electron diffraction pattern and the g-vector that were used to choose the appropriate imaging conditions. The imaging conditions were adjusted so that a Moiré pattern from the interference between the (022) planes of the PbTe and PbSe was obtained. By analysis of the crystallography, it can be noted that the Moiré pattern is essentially parallel in character. In this case, the relation for the spacing of the Moiré pattern simplifies to

$$D = d_1 d_2 / (d_1 - d_2) \quad (2.2)$$

The Moiré pattern can therefore be used for a direct determination of the spacing of the PbSe (022) lattice planes since the PbTe (022) lattice planes are assumed to be fully relaxed with no strain. Hence, we

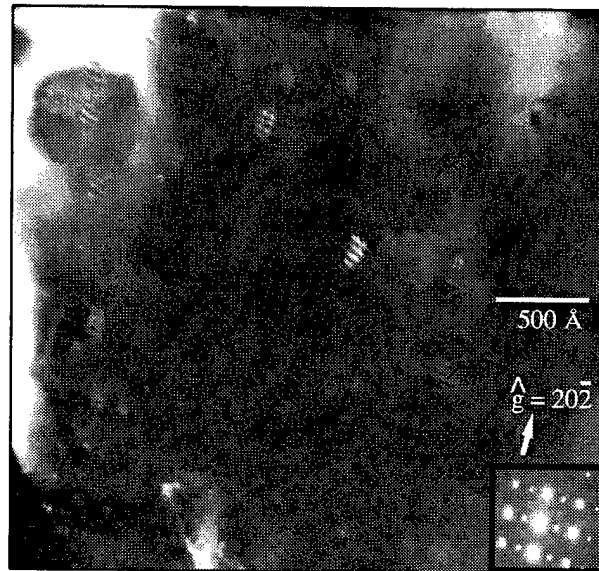


Figure 2-1. Cross-sectional centered-dark-field transmission electron micrograph of a heterostructure quantum-dot array. The Moiré patterns, obtained by interference between the quantum-dot and matrix lattice planes, are visible as bright parallel lines within the matrix material.

obtain a measure of the state of misfit strain relaxation of the PbSe quantum-dot material. For the present case, we find that the PbSe quantum-dot heterostructures have undergone essentially complete strain relaxation. That is, the spacing of the PbSe (022) lattice planes is measured to be that of unstrained PbSe. This interesting result demonstrates the utility of the present Moiré analysis for the determination of the state of misfit strain relaxation in quantum-dot heterostructures. Further, because there is typically a large distribution in size of the S-K islands of the quantum-dot heterostructure, we are currently extending the present Moiré pattern analysis using the three-dimensional critical thickness criterion described by Luryi and Suhir [3].

P. J. Taylor	T. C. Harman
D. L. Spears	M. P. Walsh
P. M. Nitishin	R. L. Slattery

REFERENCES

1. T. C. Harman, P. J. Taylor, D. L. Spears, and M. P. Walsh, *J. Electron. Mater.* **29**, L1 (2000).
2. P. Hirsch, A. Howie, R. Nicholson, D. Paschley, and M. Whelan, *Electron Microscopy of Thin Crystals* (Butterworths, London, 1965), p. 364.
3. S. Luryi and E. Suhir, *Appl. Phys. Lett.* **49**, 140 (1986).

3. SUBMICROMETER TECHNOLOGY

3.1 INTERFERENCE LITHOGRAPHY AT 157 nm

Optical lithography at 157 nm has emerged as the preferred technology for the 100–70-nm node [1]. In a relatively short time, significant progress has been made in confronting the obstacles to the implementation of this technology [2],[3]. However, this progress, particularly in the area of resist and process development, has been slowed by the lack of high-resolution exposure tools. Current fielded tools include a home-built microstepper at MIT Lincoln Laboratory, along with several other microsteppers now coming on line. These tools suffer from a relatively small field size, low numerical aperture (0.5–0.7), and aberrations which limit printing to dense features above 100 nm. These systems also are not ideally suited for resist development, because they do not easily enable the decoupling of optical performance from intrinsic resist properties.

Interference lithography [4],[5] provides a straightforward means of printing dense 50-nm features over large areas. In interference lithography the intersection of two coherent laser beams at a surface creates a sinusoidal intensity profile:

$$I(x) = 2I_0[1 + \cos(4\pi x \sin \theta / \lambda)] \quad (3.1)$$

where I_0 is the intensity of each beam (assumed to be equal), 2θ is the angle of intersection of the beams (see Figure 3-1), and λ is the laser wavelength. The nonlinear response of a photoresist can then transform this aerial image into a pattern of lines and spaces. Interference lithography has several advantages, including an essentially unlimited field size, a subwavelength spatial period

$$\Lambda = \frac{\lambda}{2 \sin \theta} \quad (3.2)$$

and, particularly important for the present effort, simple optical design with no curved optics.

Interference lithography at 157 nm presents challenges not faced at longer wavelengths where highly coherent sources are available. Because of the short (~ 10 – $50 \mu\text{m}$) spatial coherence of the F_2 laser, the wavefronts of the two beams at the sample surface must overlap to within this coherence length. Previous systems using such quasi-coherent light for achromatic interference lithography have relied on interferometers based on gratings, which must be period matched to within parts-per-million levels [6],[7]. Our setup, shown in Figure 3-1, avoids these tight tolerances with a design similar to a Jamin interferometer [8],[9]. The incoming beam is split into two arms by reflection and refraction from two rectangular CaF_2 plates. The two arms are then reflected from Si mirrors to recombine on the surface of a resist-covered substrate. The nominal angle of intersection, $\theta = 60^\circ$, yields a predicted period of 91 nm [Equation (3-2)]. The field size is limited by the input aperture of the system with a maximum of $\sim 8 \text{ mm}^2$. The angle of the final Si mirrors can be adjusted to align the beams at the resist surface. Coarse alignment is accomplished by placing a $100\text{-}\mu\text{m}$ pinhole in the beam and merging the two arms visualized on a trans-

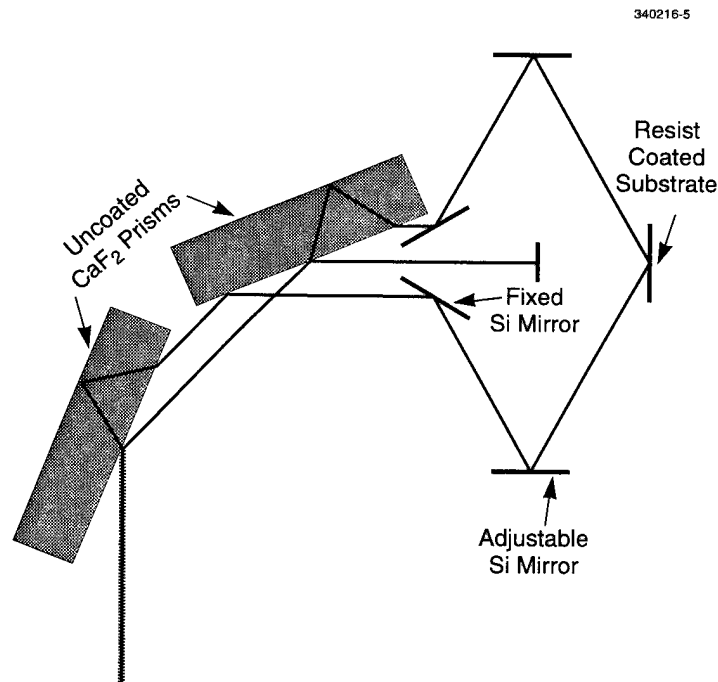


Figure 3-1. Optical schematic of the interference lithography system; all components are uncoated. The output of a 157-nm laser enters from the bottom and is split into two arms by the CaF_2 plates. The arms then reflect off Si mirrors and intersect at the sample surface. Alignment of the two beams is achieved by adjusting the angle of the final mirrors.

parent fluorescent screen. Fine alignment is determined by imaging in photoresist. The total transmission of the system, $\sim 0.24\%$, could easily be increased with reflective coatings on the Si mirrors and the back surfaces of the CaF_2 plates.

Scanning electron micrographs of samples exposed in this system are shown in Figures 3-2 through 3-6. The samples consist of a commercial deep-ultraviolet (DUV) resist (UV6, Shipley) on Si. Because this resist absorbs strongly at 157 nm (absorbance = $6.9/\mu\text{m}$), a layer only 50-nm thick was used. Figure 3-2 shows a line-and-space pattern with a period of 94 nm and approximately equal lines and spaces. Note that there is very little line edge roughness, indicating that the intrinsic performance of acid-catalyzed resists may meet critical dimension (CD) control requirements at this feature size. The line-and-space pattern was visible over extended areas, as shown in Figure 3-3. While not entirely uniform over the exposed area, the

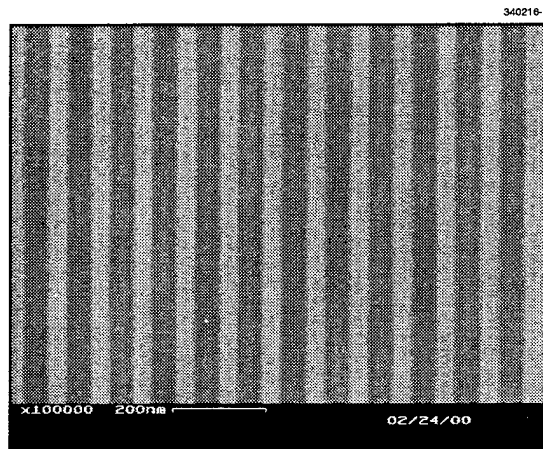


Figure 3-2. Scanning electron micrograph of a 50-nm-thick deep-ultraviolet resist (UV6), exposed with the 157-nm interference lithography tool. The period is 94 nm. Note the minimal line edge roughness.

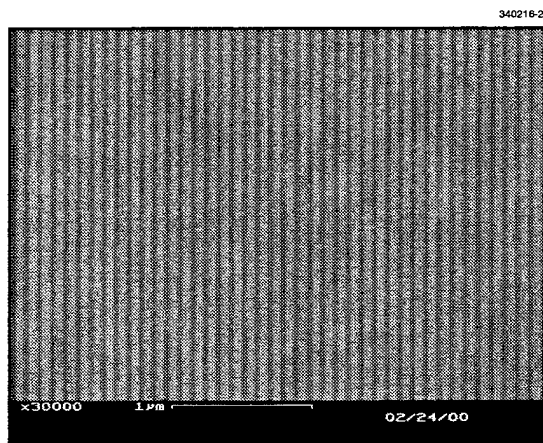


Figure 3-3. Expanded view of Figure 3-2 showing the same 94-nm period pattern extending over $10 \mu\text{m}^2$. The pattern is visible over the whole exposed area.

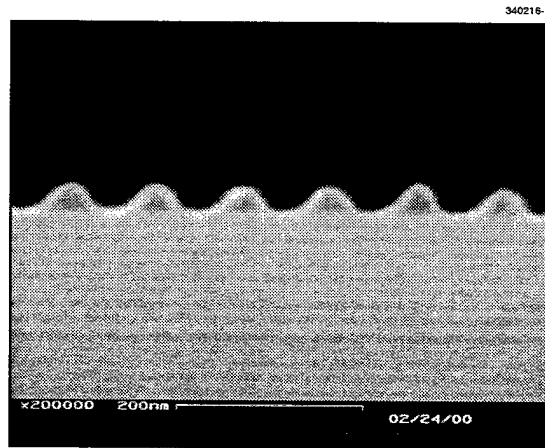


Figure 3-4. Cross-sectional view of patterned resist. These are patterns obtained in the very first exposures with our interference lithography system. The cross-sectional profiles indicate that further system and process optimization is required.

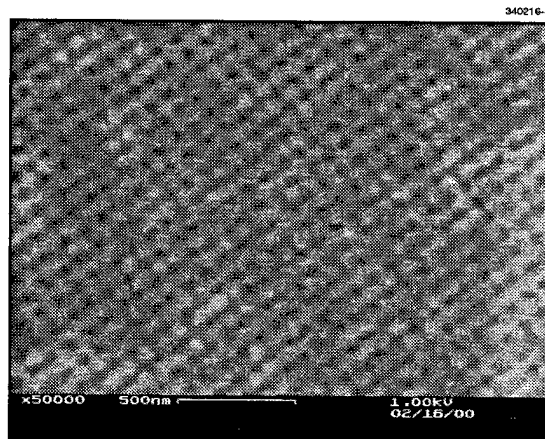


Figure 3-5. Multiple exposures can create patterns that are more complex than lines and spaces. This image was obtained with two exposures crossed at $\sim 90^\circ$.

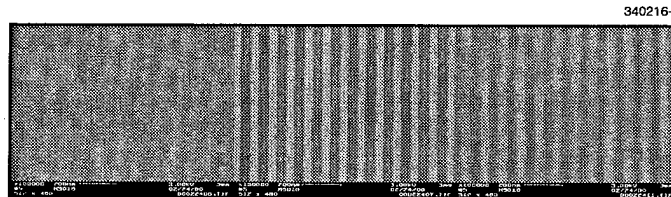


Figure 3-6. The interference pattern is sensitive to the spatial coherence of the laser. Contrast increases and then decreases again as one arm is translated with respect to the other. Each micrograph represents an additional translation of 18 μm . The results provide an estimate of the spatial coherence length of the F_2 laser.

pattern was found in every area of the $\sim 0.75\text{-mm}^2$ field that was examined. Figure 3-4 shows a cross-sectional view of the exposed pattern. We note that these were among the very first exposures obtained on our system. The rounded profiles indicate that further optimization of the optics and of the resist processing is needed. We expect that ongoing improvements to the system will allow better alignment and thus a better aerial image. Finally, interference lithography is not limited to simple line-and-space patterns. Figure 3-5 shows a lattice pattern of $\sim 50\text{-nm}$ -diam openings in resist, formed by two crossed exposures. Additional exposures, along with the introduction of a mask, can be used to create arbitrary patterns with interference lithography [10],[11].

While sensitivity to the spatial coherence of the F_2 laser presents special difficulties for interference lithography at 157 nm, it also provides a means to measure the laser coherence length. Figure 3-6 shows micrographs that result from translating one beam with respect to the other. In the left image the contrast of the interference pattern is very low. Translating one beam 18 μm yields a high contrast pattern (center image), and a second 18- μm translation results in another low contrast image (right image), providing a rough estimate of the laser spatial coherence length, $\sim 40 \mu\text{m}$.

Development of 157-nm interference lithography is ongoing, and the results reported here are only preliminary. Nevertheless, they already indicate that such a system is very useful for sub-100-nm resist development, as well as for process development at those dimensions (such as pattern transfer), and for the fabrication of specialized devices.

M. Switkes
T. M. Bloomstein
M. Rothschild

3.2 ENCAPSULATED INORGANIC RESIST TECHNOLOGY

All manufacturing of integrated circuits has been enabled by high-performance spin-on organic polymeric resists, but resolution in traditional single-layer organic resists has been limited by the inability to image at aspect ratios (resist height to image width) of much greater than 3:1. As critical features approach 25 nm, resist thickness is expected to drop to under 100 nm, a thickness that does not allow plasma image transfer into underlying layers even with a several-fold improvement in plasma etch selectivity. For lithography to continue to enable integrated circuit manufacture, either this limiting 3:1 aspect ratio must be broken or plasma etch resistance must be improved by an order of magnitude. Multilayer resist schemes offer the capability of increased aspect ratio, but they add to the process complexity and cost [12]–[17]. We have studied encapsulated inorganic materials as resist components with the goal of developing a proof-of-concept resist system ultimately capable of sub-100-nm resolution with sufficient plasma etch selectivity. These resist systems will act as a single-layer hard mask compatible with existing resist processing steps.

Encapsulated inorganic resist technology (EIRT) produces a fundamentally new type of resist material, which will be compatible with conventional resist processing such as spin casting from organic solvents and development with aqueous 2.38% TMAH developers. A key feature of the resist is the use of encapsulated inorganic materials as resist components, a fact that significantly increases the plasma etch selectivity of EIRT resists compared to conventional polymeric resists. In effect, these resist systems will act as a photoimagable single-layer hard mask, although use as the top layer in a bilayer resist scheme is certainly possible.

Our goal of developing a proof-of-concept resist system ultimately capable of sub-100-nm resolution with high plasma etch selectivity required that the EIRT resists be capable in the wide array of advanced imaging schemes currently under consideration for nanometer lithography. These resists have the potential to be imaged under a variety of advanced imaging techniques such as X-rays, extreme ultraviolet, low- and high-kV electrons, and extended optical wavelengths, but for our proof-of-concept we will just show examples of imaging with 50-kV electron beams.

Initial lithography using EIRT materials was performed with electron beam imaging and the results are compared with Shipley UV5, a commercial DUV resist, based on traditional organic polymers, that has shown promise as an electron beam resist. The SiO_2 -containing resists, formulated to be similar to UV5, were prepared to contain 20, 33, and 50% 10–20-nm-diam SiO_2 nanoparticles (weight SiO_2 to weight of total solids). As shown in Figure 3-7, the resists containing 33 and 50% SiO_2 exhibit increased dark loss and reduced resist contrast when compared to UV5. The increased sensitivity relative to UV5 is likely to be a result of the lower level of dissolution inhibition of these two resists compared to UV5. What is somewhat surprising is that the resist containing 20% SiO_2 had a bulk lithography performance identical to that of UV5 in terms of sensitivity, contrast, and dark loss. Thus, at levels of 20% added SiO_2 , the lithography is little changed from that of a resist not containing the SiO_2 nanoparticles.

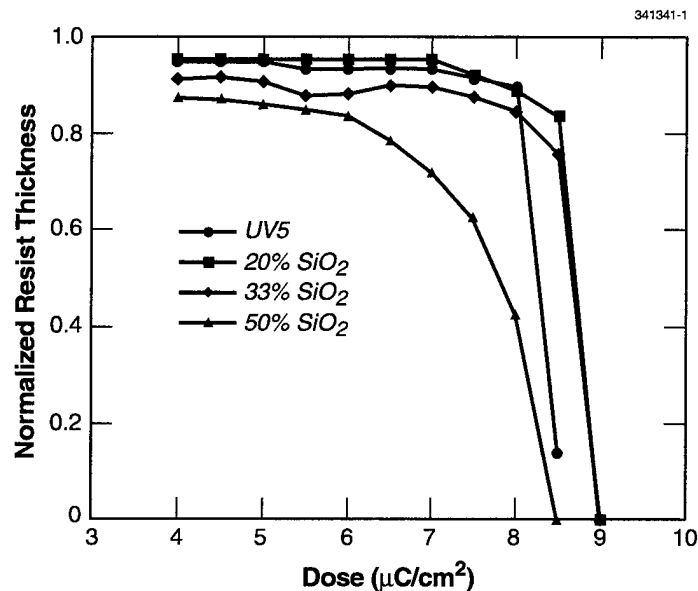


Figure 3-7. Comparison of contrast curves of encapsulated inorganic resist technology (EIRT) resists and the commercial resist UV5 with 50-kV electron beam exposure.

The effect of adding 20% SiO₂ nanoparticles to a resist on actual resist imaging performance was determined. Figure 3-8 shows scanning electron micrographs (SEMs) of the electron lithography of UV5 and a similar resist containing 20% SiO₂ nanoparticles. The 200- and 300-nm dense and isolated lines were the smallest features written and evaluated with our electron beam pattern. The SEM images show that little difference exists in either resolution or resist profiles between the UV5 and the SiO₂-containing resist. This initial imaging result was very encouraging and prompted a study to evaluate the effect of added SiO₂ on plasma etch resistance and also to determine what level of SiO₂ in the resist is needed to substantially improve the plasma etch resistance of the resist.

The reactive ion etch (RIE) rates of resists containing 10, 20, 33, and 50% SiO₂ nanoparticles were compared to UV5 and a film of pure SiO₂ nanoparticles. The results of etching the six films in both oxygen and chlorine plasma are seen in Figure 3-9 and summarized in Table 3-1. The improvement in plasma etch resistance is most dramatic in the oxygen RIE plasma where even the addition of only 10% SiO₂ decreases the plasma etch rate by half. More important, the incorporation of 20% SiO₂, an amount that gives electron beam imaging similar to UV5, reduces the plasma etch rate to a quarter of the original rate. It is clear that as SiO₂ content is increased further, the etch rate in an oxygen plasma continues to decrease. This reduction in plasma etch rate will translate to a 4–20 times improvement in plasma etch selectivity over UV5 at SiO₂ levels of 20–50%.

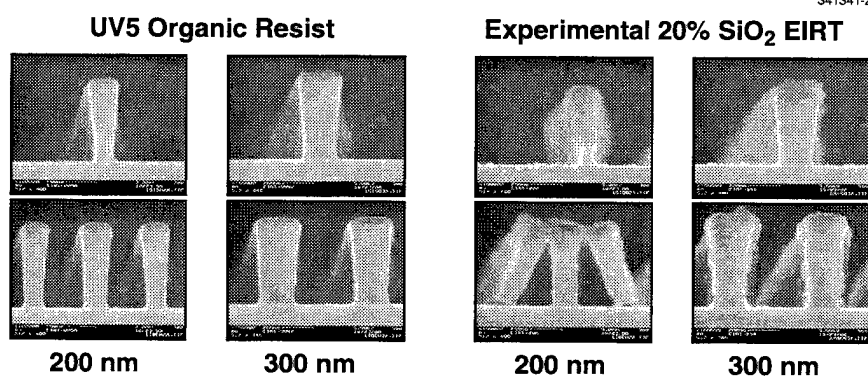


Figure 3-8. Comparison of electron beam imaging of 200- and 300-nm dense and isolated lines of an EIRT resist and the commercial resist UV5.

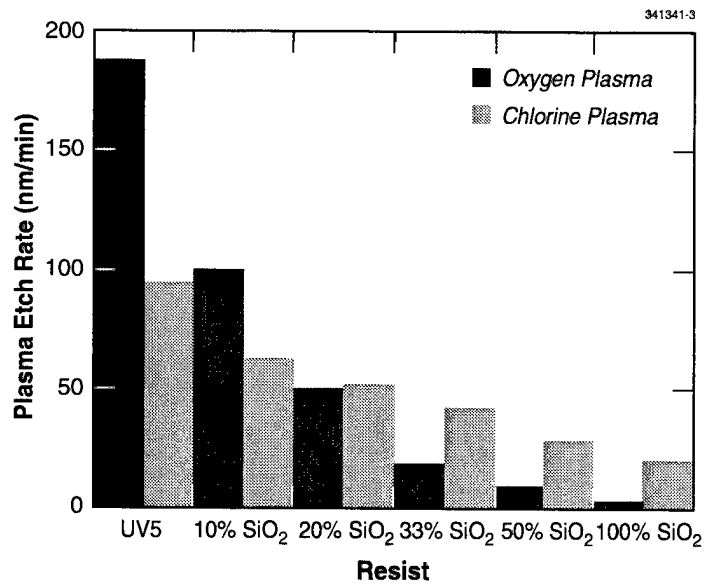


Figure 3-9. Comparison of reactive ion etch rates of resists containing increasing amounts of SiO₂ in both an oxygen and chlorine plasma.

TABLE 3-1
Comparison of RIE Etch Rates of Resists in Oxygen and Chlorine Plasmas

Resist	Percent SiO ₂	Oxygen Etch Rate (nm/min)	Chlorine Etch Rate (nm/min)
UV5	0%	188	95
10% SiO ₂ Resist	10%	100	63
20% SiO ₂ Resist	20%	50	52
33% SiO ₂ Resist	33%	18	42
50% SiO ₂ Resist	50%	9	28
SiO ₂	100%	3	20

The chlorine plasma etch rate also decreases with increasing levels of SiO₂ incorporation into the resist. The addition of 20% SiO₂ to the resist will lower the chlorine RIE etch rate by half, and incorporation of 50% SiO₂ into the resist will reduce the etch rate to a third. It should be noted that both the oxygen and chlorine plasmas were run at relatively high dc bias of -460 and -370 V and thus have a significant nonselective sputter etch component. Plasma etch process optimization could lead to further improvements in etch selectivity of the SiO₂ resists over a traditional polymeric organic resist.

These results, combined with the previous electron beam results, constitute a proof-of-concept that resists developed from the EIRT concept can both image similarly to a commercial resist and exhibit improved plasma etch resistance. This makes the EIRT resist concept a candidate for both single-layer resists and the top imaging layer of bilayer resist schemes. Furthermore, the use of transparent SiO₂ nanoparticles makes the EIRT resist system especially useful for sub-200-nm wavelength optical exposure systems, especially 193 and 157 nm, where improved plasma etch resistance can be imparted by the use of the thicker transparent EIRT resists.

T. H. Fedynyshyn E. Matijevic
S. P. Doran I. Sondi
M. L. Lind

REFERENCES

1. M. Rothschild, T. M. Bloomstein, J. E. Curtin, D. K. Downs, T. H. Fedynyshyn, D. E. Hardy, R. R. Kunz, V. Liberman, J. H. C. Sedlacek, R. S. Uttaro, A. K. Bates, and C. Van Peski, *J. Vac. Sci. Technol. B* **17**, 3262 (1999).
2. T. M. Bloomstein, M. W. Horn, M. Rothschild, R. R. Kunz, S. T. Palmacci, and R. B. Goodman, *J. Vac. Sci. Technol. B* **15**, 2112 (1997).
3. T. M. Bloomstein, M. Rothschild, R. R. Kunz, D. E. Hardy, R. B. Goodman, and S. T. Palmacci, *J. Vac. Sci. Technol. B* **16**, 3154 (1998).
4. E. H. Anderson, K. Komatsu, and H. I. Smith, *J. Vac. Sci. Technol. B* **6**, 216 (1988).
5. S. H. Zaidi, S. R. J. Brueck, F. M. Schellenberg, R. S. Mackay, K. Uekert, and J. J. Persoff, *Proc. SPIE* **3048**, 248 (1997).
6. T. A. Savas, M. L. Schattenburg, J. M. Carter, and H. I. Smith, *J. Vac. Sci. Technol. B* **14**, 4167 (1996).
7. E. N. Leith and B. J. Chang, *Appl. Opt.* **12**, 1957 (1973).
8. M. Born and E. Wolf, *Principles of Optics*, 3rd ed. (Pergamon, London, 1965), pp. 309–310.
9. J. Jamin, *C. R. Acad. Sci. (Paris)* **42**, 482 (1856).
10. X. Chen and S. R. J. Brueck, *Proc. SPIE* **3331**, 214 (1997).
11. X. Chen and S. R. J. Brueck, *J. Vac. Sci. Technol. B* **16**, 3392 (1998).
12. J. R. Havas, *Electrochem. Soc. Ext. Abstr.* **2**, 743 (1976).
13. J. Shaw, E. Babich, M. Hatzakis, and J. J. Paraszczak, *Solid State Technol.* **30**, 83 (1987).
14. M. Hatzakis, *Solid State Technol.* **24**, 83 (1981).
15. Y. Ohnishi, M. Suzuki, K. Saigo, Y. Saotome, and H. Gokan, *Proc. SPIE* **539**, 62 (1985).
16. A. S. Gozdz, *Solid State Technol.* **30**, 75 (1987).
17. E. Reichmanis, G. Smolinsky, and C. W. Wilkons, *Solid State Technol.* **28**, 130 (1985).

4. BIOSENSOR AND MOLECULAR TECHNOLOGIES

4.1 EFFECT OF ENVIRONMENTAL CONTAMINANTS ON THE SURVIVABILITY OF ENGINEERED B CELLS USED IN A BIOELECTRONIC SENSOR

The development of CANARY (Cellular Analysis and Notification of Antigen Risks and Yields), a novel bioelectronic sensor to detect and identify pathogens, has been previously described [1]–[3]. One of the key elements of the sensor is an immortalized B cell, a type of white blood cell. The B cells have been genetically engineered to express three genes: two result in expression of an antibody on the surface of the B cell capable of recognizing and binding a specific antigen (i.e., viruses or bacteria), and one produces a protein that emits photons in response to the specific binding of the antigen to the antibody.

This cell-based biosensor will be used in the field to warn of pathogens in the environment. However, under sampling conditions, the sensor will also be exposed to a vast assortment of common environmental contaminants. The B cell must not only be able to withstand the assault of potentially toxic substance but also retain its ability to function specifically in response to antigens. A series of dose-response and duration of exposure experiments were designed to test the robustness of the B cells in the presence of several potential field-condition contaminants.

The design of the microfluidic sensor is such that the cells will be exposed to soluble and insoluble microscopic components in air samples, rather than macroscopic particles. Therefore, to more closely simulate actual operating conditions of the sensor, soluble and $<0.2\text{-}\mu\text{m}$ particulate contaminants were extracted from chimney soot, urban particulate matter, and several types of soil. Diesel exhaust fumes were collected onto dispersed cellulose matrices using an air sampler at a flow rate of 1.0 L/min for 2, 6, 11, and 15 min prior to extraction. B-cell viability determined before and after exposure to various concentrations of the contaminants is shown in Figure 4-1. After 24 h of continuous exposure to chimney soot or urban particulate matter [Figure 4-1(a)] or diesel exhaust [Figure 4-1(b)], the B cells were found to be extremely resistant to all but the highest concentrations of contaminant. Additionally, a tenfold dilution of diesel exhaust and chimney soot and a 100-fold dilution of urban particulate matter samples were sufficient to restore viability to a level comparable to controls. Figure 4-1(c) shows that of the four different types of soil tested—montmorillonite, silt loam, clay loam, and barnyard muck—cell viability was unaffected, even after 72 h of exposure to nearly saturated extracts.

Since length of exposure might influence the degree of toxicity and thereby impact sensor design and operation, we investigated how duration of exposure affected viability. Figure 4-2 shows the results of a washout experiment which revealed that viability was reduced only 50% if high concentration diesel contaminants were removed after 4 h of exposure, compared to a 99% loss of viability if exposure lasted 24 h or longer.

Results from these experiments indicate that the B cells are extremely robust at all but the highest concentrations of contaminants. Additionally, these studies were all designed to simulate the worst

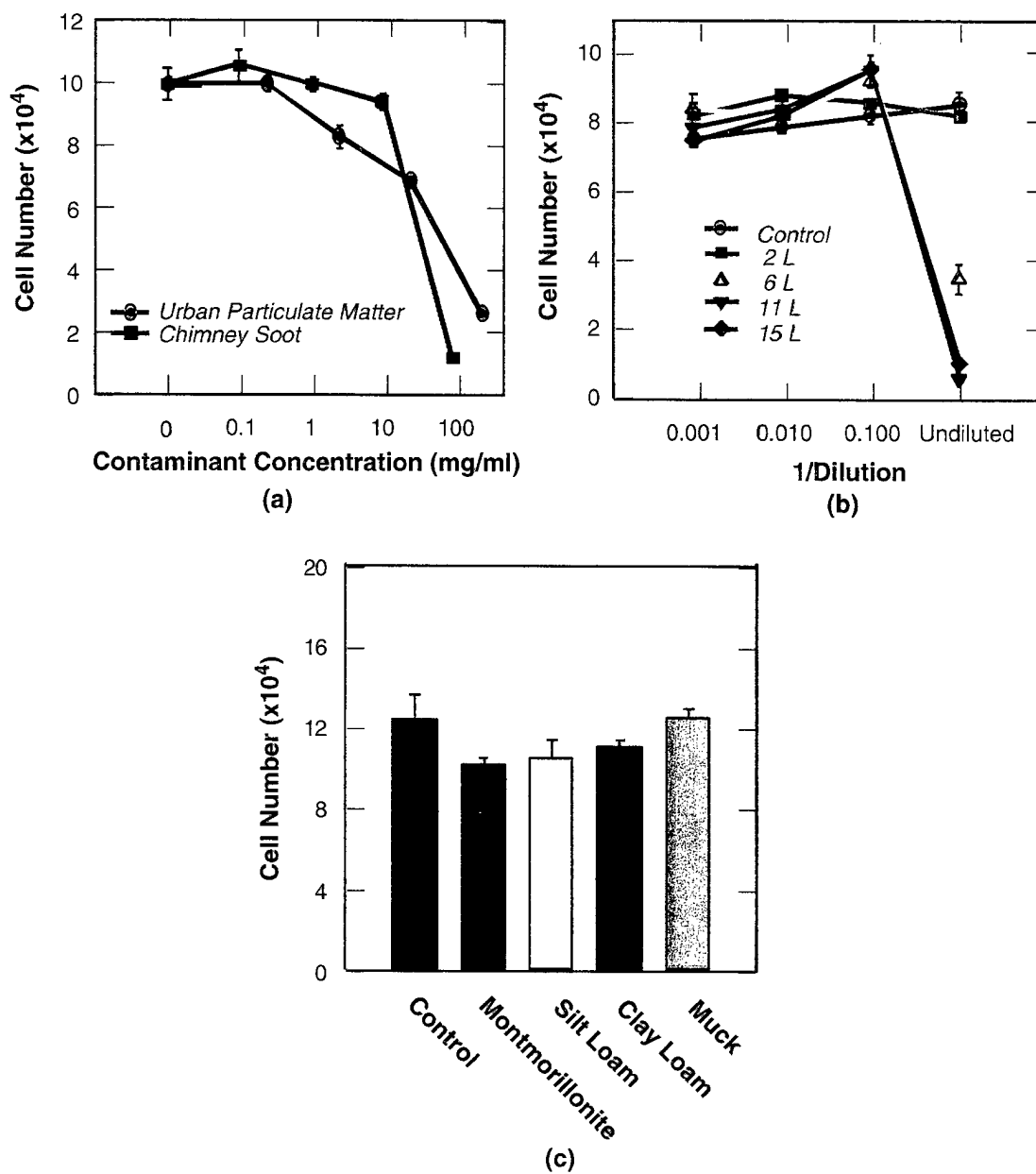


Figure 4-1. Viability of B cells in the presence of contaminants. Dose-response of cells after exposure to (a) urban particulate matter and chimney soot extracts, (b) diesel exhaust extracts for 24 h at 37°C, and (c) saturated solutions (125–250 mg/ml) of soil extracts for 72 h at 28°C.

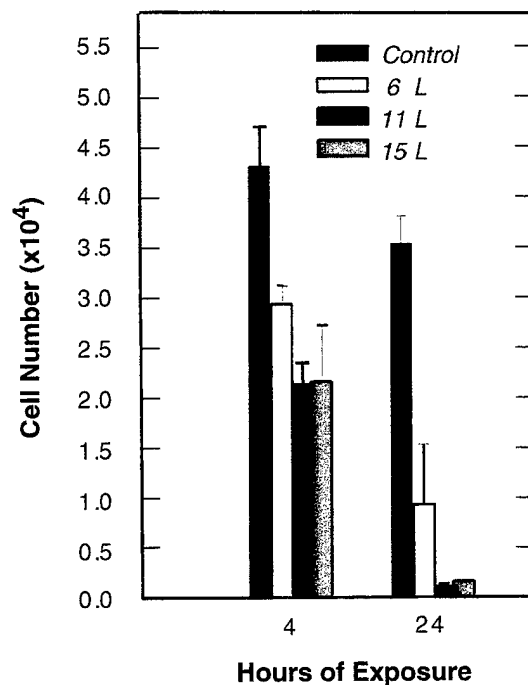


Figure 4-2. Undiluted extracts from control, 6-, 11-, and 15-L samples were added to B cells at time zero. Contaminants were removed and replaced with fresh media after 4 and 24 h of exposure at 28°C. Viability was assayed at 72 h from the start of the experiment.

possible conditions, using extremely high concentrations of and long exposures to contaminants. It is unlikely that cells in the sensor will be exposed to levels and durations where toxicity will be a factor. However, being aware of the limitations of the cells will give a much clearer indication of how the biosensor can be designed and operated to minimize or even eliminate deleterious effects from environmental contaminants.

These experiments were carried out under standard culture conditions in the laboratory. Future plans include studies to expand these findings to the behavior of the cells in the sensor, in order to test robustness and the ability to maintain functionality in the presence of contaminants and to verify that contaminants do not induce nonspecific luminescence of the cells.

F. E. Nargi
T. H. Rider
M. A. Hollis

M. S. Petrovick
A. M. Young
J. Chen

REFERENCES

1. Solid State Research Report, Lincoln Laboratory, MIT, 1998:4, p. 27.
2. Solid State Research Report, Lincoln Laboratory, MIT, 1999:1, p. 21.
3. Solid State Research Report, Lincoln Laboratory, MIT, 1999:2, p. 21.

5. ADVANCED IMAGING TECHNOLOGY

5.1 DEVELOPMENT OF ANTIREFLECTION COATINGS FOR CCD IMAGERS

Back-illuminated charge-coupled device (CCD) imagers offer the possibility of high quantum efficiency over a broad spectral range from the uv into the near infrared. However, antireflection coatings (ARCs) must be applied to the back surface of such devices in order to minimize reflection losses and couple the maximum amount of radiation into the detector. For most applications, such as surveillance, night vision, or astronomy, these coatings should minimize reflection losses over the broadest wavelength range possible. However, the ARC can also reduce multiple internal reflections (Fabry-Perot effect) in the near infrared in thinned imagers. We describe here some results on one- and two-layer coatings and their impact on quantum efficiency and Fabry-Perot effects.

The selection of materials suitable for ARCs on a CCD is somewhat limited because of various constraints. Because of its relatively large refractive index, silicon requires high-index films, either singly or in combination with a second lower-index film, for optimum matching. The sensitivity of the CCD to ionizing radiation precludes film deposition by e-beam or sputtering techniques, which are often the best methods for depositing certain materials. We have used thermal evaporation exclusively, although we have begun experiments with ion-assisted deposition. The latter can lead to denser films with characteristics closer to the bulk properties of the materials.

Three high-index materials that offer good performance on silicon are TiO_2 , SiO , and HfO_2 . These can be used singly or in combination with lower-index materials in two-layer coatings for broader wavelength matching. The starting point for designing coatings is to compute the reflectance vs wavelength and select film thicknesses that minimize reflectance over the desired band. Figure 5-1 shows three examples of such calculations. The single-layer HfO_2 and SiO coatings were originally selected for narrowband applications and designed for minimum reflectance at 400 and 600 nm, respectively, but, as would be expected of single-layer coatings, they do not offer low reflectance across a wide bandwidth. The $\text{TiO}_2/\text{Al}_2\text{O}_3$ coating was studied with the goal of achieving better performance across the range from 400 to 1000 nm. It would also be desirable to attain good quantum efficiency into the uv, but this is difficult for two reasons. First, the high dispersion of silicon in the range 200–400 nm makes it difficult to match with the available films. Second, the back surface treatment currently used in our imagers leads to relatively high photoelectron losses in this regime, so the quantum efficiency would be low in any case. Another coating currently in use is the combination $\text{HfO}_2/\text{SiO}_2$. Its reflectance spectrum on silicon is similar to that of the $\text{TiO}_2/\text{Al}_2\text{O}_3$ results in Figure 5-1.

Figure 5-2 shows the quantum efficiency of devices with each of these films. The light source for these measurements was a monochrometer with its slits set at maximum opening (maximum bandwidth) to suppress the interference effects described below. Further, all measurements were done at -50°C , with the exception of the $\text{HfO}_2/\text{SiO}_2$ -coated device. The HfO_2 , as expected, does well in the blue, and the SiO in

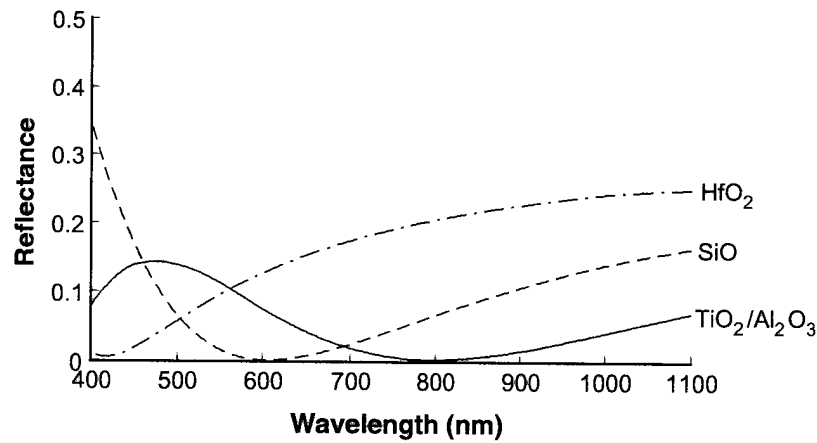


Figure 5-1. Calculated reflectance vs wavelength for three coatings on a semi-infinite silicon substrate. The HfO_2 film was 48 nm and the SiO 80 nm. For the two-layer coating, the TiO_2 was 160 nm and the Al_2O_3 350 nm.

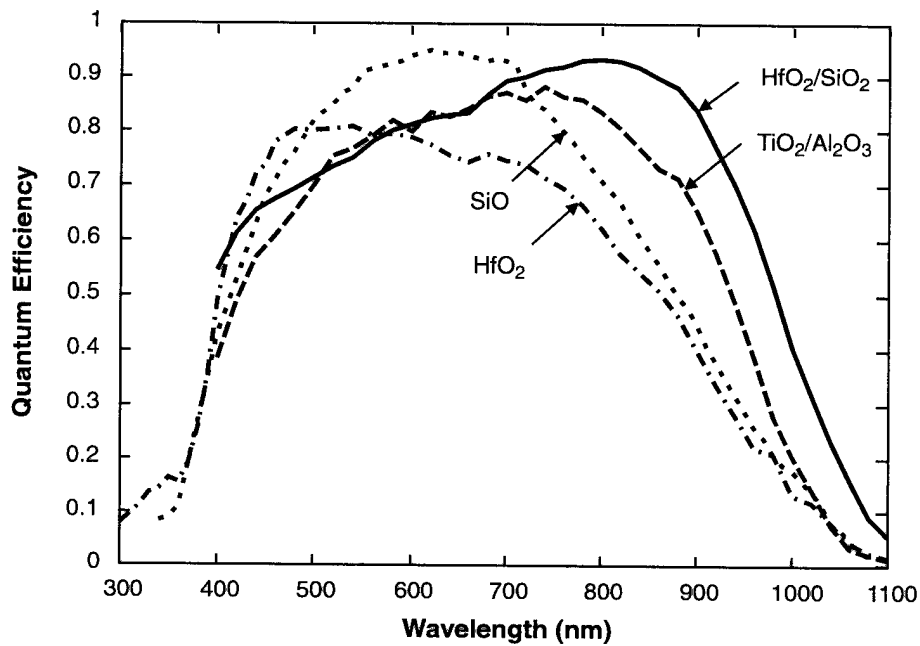


Figure 5-2. Measured quantum efficiency on back-illuminated CCDs with various coatings. All the data was taken at a device temperature of -50°C with the exception of the $\text{HfO}_2/\text{SiO}_2$ case, which was at room temperature.

the visible, while the dual-layer coatings have somewhat broader responses. One advantage of the two-layer coatings in the near infrared is attributable to better matching as discussed earlier, but in addition the devices themselves are about 40–50 μm thick in comparison with 10–20 μm for the devices with the single-layer coatings. At the shorter wavelengths the SiO data falls rapidly toward 400 nm owing to absorption in the film. The $\text{Al}_2\text{O}_3/\text{TiO}_2$ is somewhat worse in the blue-green than the $\text{SiO}_2/\text{HfO}_2$, even though in theory it should do better. The problem with the former is that we found it difficult to deposit TiO_2 and Al_2O_3 by evaporation while maintaining stoichiometry. These films tend to be metal-rich, which leads to high absorption losses, unless deposited in a high back pressure of O_2 . HfO_2 and SiO_2 , on the other hand, do not have this problem, and for this reason we now use this combination as our standard broadband coating.

One annoying problem astronomers face in using thinned back-illuminated CCDs arises from the Fabry-Perot effects in the range from approximately 800 to 1100 nm. In this wavelength band, the optical absorption coefficient in silicon is longer than typical device thicknesses, which leads to multiple internal reflections and corresponding oscillations in device quantum efficiency. This effect is not apparent in the data of Figure 5-2 because the monochromator used in those measurements had its slits set for a bandwidth greater than the period of the oscillations. Another aspect of this problem is that because of device thickness variations, the quantum efficiency can also vary strongly as a function of position on the device. This effect can be dramatically seen in sky images where the narrowband sky glow emission from OH ions in the upper atmosphere [1] produces Newton's rings in the imagery. It is usually difficult and laborious to remove such artifacts by flat fielding or pixel-by-pixel calibration techniques.

We have been able to minimize these effects by placing a reflectance minimum of the ARC in the near infrared, as shown in Figure 5-1 for the case of the $\text{TiO}_2/\text{Al}_2\text{O}_3$ coating. The Fabry-Perot interference effects have been measured on devices with the various ARCs, and the results are shown in Figures 5-3 and 5-4. In this case, the CCD response is measured as a function of wavelength using the collimated output of a monochromator whose bandwidth is set to 0.5 nm. Figure 5-3 shows plots of the relative deviation of the photoresponse from the mean. The principle oscillations have a period corresponding to multiple reflections within the thin silicon membrane. For a device thickness T , the period of these oscillations is $\lambda^2/2nT$, where n is the refractive index of silicon. This yields periods of about 6 nm for the devices shown here. A second, longer-period oscillation of a few 10's of nm can be seen in some cases, and we believe this results from the epoxy bonding layer used to attach the thinned CCD to its support wafer.

Figure 5-4 shows the peak-peak response deviation from Figure 5-3 as a function of wavelength. The two-layer coating is clearly superior as expected. It should be noted that these results are "worst case" in the sense that they represent pure collimation and a limiting narrow bandwidth. In real optical systems with finite focal ratios the interference effect would be reduced.

B. E. Burke	J. A. Gregory
C. C. Cook	T. A. Lind
A. H. Loomis	P. W. O'Brien

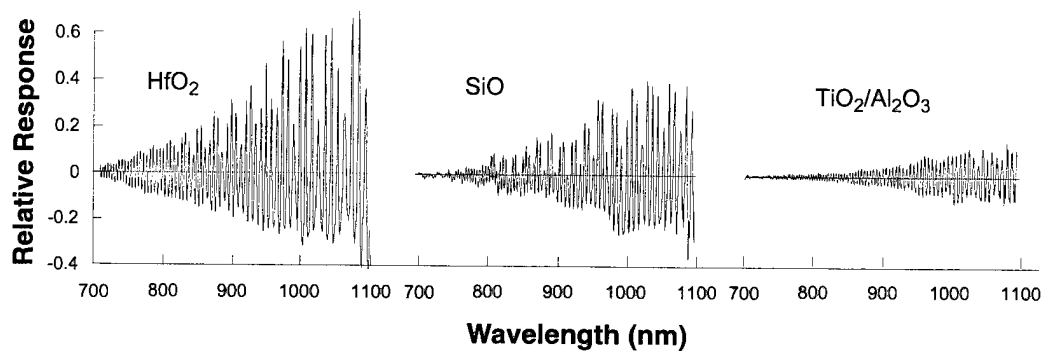


Figure 5-3. Plots of the Fabry-Perot interference effects on three devices in the near infrared using narrowband collimated light.

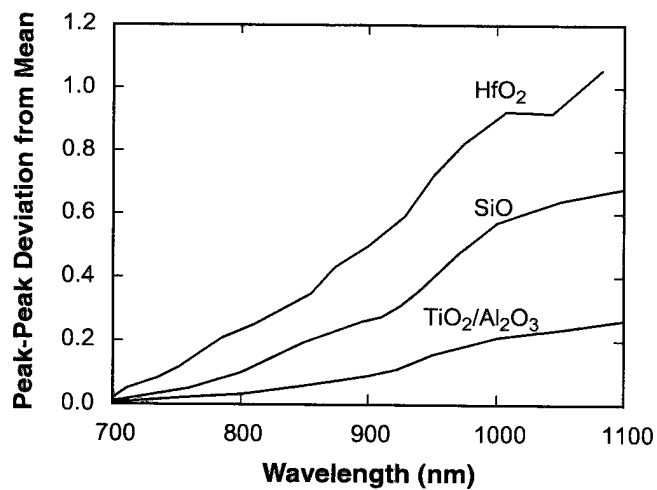


Figure 5-4. Peak-peak deviation of the device response due to fringing as a function of wavelength for the three devices of Figure 5-3.

REFERENCE

1. A. L. Broadfoot and K. R. Kendall, *J. Geophys. Res.* **73**, 426 (1968).

6. ANALOG DEVICE TECHNOLOGY

6.1 WIDEBAND PHOTONIC PHASED-ARRAY BEAMFORMER DESIGN

For well over a decade, rf/photonic techniques [1],[2] have been under development for realizing wideband agile-beam rf antenna systems. Much of this work has centered on phased-array systems which, compared to mechanically scanned antennas, offer important performance features including multiple independent beams, rapid scanning, and wide instantaneous bandwidth. One of the major challenges facing all phased-array antennas is reducing the size, weight, power, and cost of the complex hardware required to realize high-performance systems. We have developed beamformer designs based on rf/photonic techniques for wideband phased-array receive antennas. These designs offer order-of-magnitude reductions in weight over conventional all-rf approaches. While these beamformer designs exploit recent advances in photonic components that have been developed principally for wavelength-multiplexed fiber-optic telecommunications, continued development of analog rf/photonic components will lead to significant improvements in overall beamformer performance.

Our recent work has focused on receive phased-array antenna systems, for which a generic rf/photonic architecture is shown in Figure 6-1. The rf signal from each element or subarray modulates an optical carrier wave at the electrical-to-optical (EO) conversion element. For true-time-delay (TTD) beamforming, which is required for wideband squint-free array operation, time delays appropriate for the beampointing direction are applied to each subarray output, and the combined signal is converted back to rf in a photoreceiver. Because of its light weight, low loss, and ultrawide bandwidth, optical fiber is an ideal medium for performing the TTD function. Hybrid approaches combining rf techniques for fine-scale TTD and photonic methods for coarse TTD show particular promise. For high-performance systems, EO conversion is typically accomplished using a cw laser and external electrooptic modulator. With components available today, analog modulation bandwidths of 10's of GHz are readily achieved.

An important objective of any beamformer design is minimizing component count. The photonic beamformer architectures we have investigated work towards this objective by exploiting recent advances in optical wavelength multiplexing technology. These architectures utilize a combination of (1) spatial switching between fiber elements, and (2) wavelength-addressable delay [3]. Fiber-optic $1 \times N$ switches with low insertion loss and low crosstalk are now readily available. A photonic TTD design that combines spatial switching and wavelength addressable delay is shown in Figure 6-2. A fixed wavelength is assigned to each input, and the signals are combined through a wavelength multiplexer onto a single fiber. A $1 \times m$ switch selects a fiber Bragg grating which applies the appropriate time delay to each wavelength component. The system shown could be used for a linear array where there are m coarse TTD beam directions and k independently selected fine-scale tilt angles, thus totaling $m \times k$ beam directions. Similar designs can be configured for two-dimensional beam steering. Photonic beamformers of this type offer a large size and weight savings over all-rf designs of comparable performance.

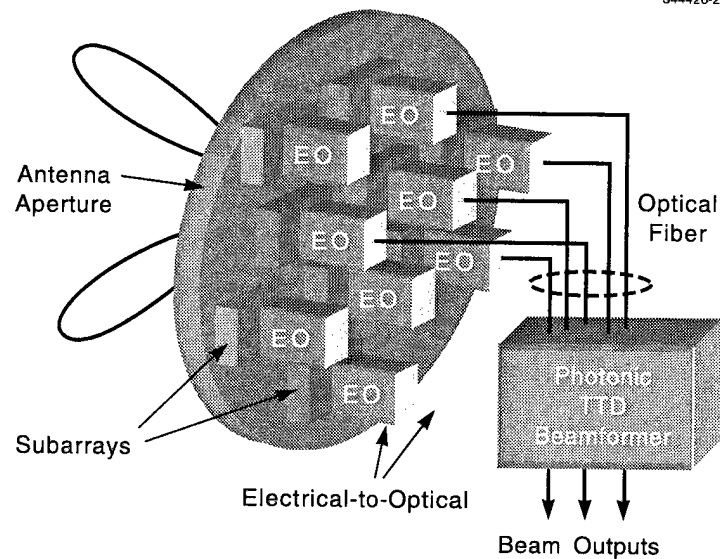


Figure 6-1. Schematic view of an rf/photonic phased-array receive antenna. Subarray rf output signals modulate an optical carrier wave (EO converter) and the signals are sent via optical fiber to a photonic true-time-delay (TTD) beamforming network. The combined signal is converted back to rf to provide the beam output.

The dc power requirements of rf-to-photonic conversion is an important system consideration for large arrays. This is particularly true for receive systems, which will typically have a large number of EO converters at the element or subarray level. To maintain a low system noise figure a drive amplifier prior to the EO modulator is typically required, with the necessary amplifier gain determined largely by the modulator sensitivity V_π , laser power, and downstream optical insertion loss. For a V_π of 4 V, which is available today, and moderate laser power, an amplifier gain of close to 30 dB is required. Depending on system dynamic range needs, which are driven by the signal environment, a single rf-to-photonic EO converter could consume in excess of 1 W with current technology. However, reducing modulator V_π to a few tenths of a volt can result in eliminating the need for a drive amplifier, thus reducing EO converter power requirements to under 100 mW.

In summary, rf/photonic techniques that exploit the small size and weight of optical fiber, the wide bandwidths of optoelectronic components, and the unique capabilities offered by wavelength multiplexing offer very significant opportunities for realizing high-performance array antenna systems.

L. M. Johnson	G. E. Betts
P. A. Schulz	P. W. Juodawlkis
W. G. Lyons	

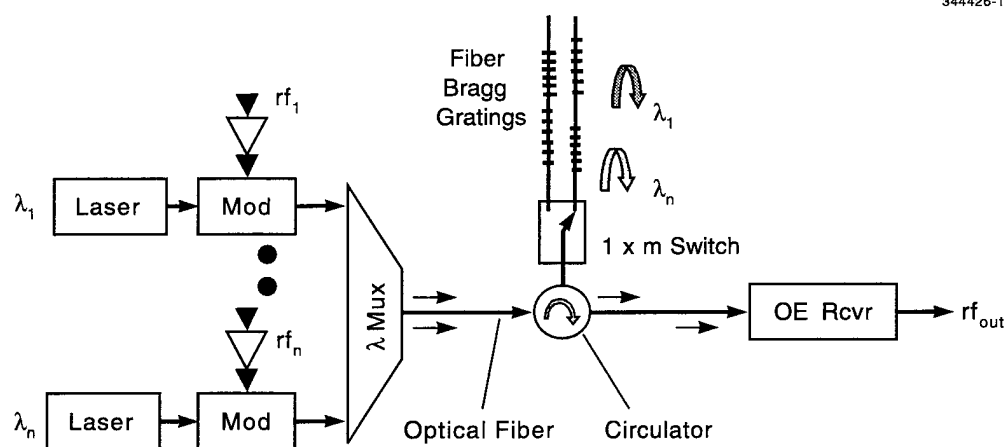


Figure 6-2. Schematic diagram showing the basic functionality of a wavelength-multiplexed TTD beamformer. Each of n rf inputs is assigned an optical wavelength and the signals are combined in a wavelength multiplexer. A $1 \times m$ spatial switch selects a fiber Bragg reflective grating that applies the appropriate time delay to each subarray signal. The combined signal is then converted back to rf in the optoelectronic receiver.

REFERENCES

1. M. Y. Frankel, P. J. Matthews, R. D. Esman, and L. Goldberg, *Opt. Quantum Electron.* **30**, 1033 (1998).
2. H. Zmuda and E. N. Toughlian, *Photonic Aspects of Modern Radar* (Artech House, Norwood, Mass., 1994).
3. D. T. K. Tong and M. C. Wu, *IEEE Trans. Microwave Theory Tech.* **46**, 108 (1998).

7. ADVANCED SILICON TECHNOLOGY

7.1 MEMS MICROSWITCHES

Two novel microelectromechanical systems (MEMS) switch designs for use in microwave circuits are under development. One of the designs is a capacitive type, shown in Figure 7-1, which incorporates a rolling cantilever and is a direct descendent of the microshutters described earlier [1]. This device can be used in microwave circuits to switch in or out components or circuit stubs in a microstrip circuit, for example. The second design is similar except that it includes a dc contact at the end of a much shorter cantilever, as shown in Figure 7-2, and makes a very compact dc switch. This microswitch can be used in the same applications as the capacitive switch and is also capable of being configured in a multi-element X-Y array, as shown in Figure 7-3, for use in a revolutionary circuit concept for a new class of reconfigurable microwave circuits and antennas. The switches within the array can be individually actuated, which provides the means to modify the circuit trace and therefore allows fine tuning or complete reconfiguration of circuit element behavior. Device performance can be reconfigured over a decade in bandwidth in the nominal frequency range 1–100 GHz. In addition, other circuit element attributes can be reconfigured, such as instantaneous bandwidth, impedance, and antenna polarization. This will enable the development of next-generation communication, radar, and surveillance systems with the ability to reconfigure operation for diverse operating bands, modes, power levels, and waveforms.

The rf microswitches are fabricated in Lincoln Laboratory's Microelectronics Laboratory using silicon CMOS processing techniques. The cantilever arm is formed from a three-layer deposition of 350-nm aluminum sandwiched between two 100-nm layers of controlled-stress silicon dioxide. The materials for the switch were chosen because silicon dioxide is strong and resilient and has low density, a low Young's modulus, and a low expansion coefficient. This combination balances the high-expansion aluminum and provides stability over temperature. The aluminum combines light weight with high electrical conductivity. The lower silicon dioxide film is deposited with controlled compressive stress while the upper film is deposited with tensile stress. In the resting state, the built-in stresses of the silicon dioxide films curl the switch cantilever away from the substrate so that the switch contact is open, and the rf impedance is high. The curling motion of the short cantilever arm allows the microswitches to be very compact, while at the same time providing a relatively large open-contact separation distance, 50 μm for the capacitive switch and $\sim 6 \mu\text{m}$ for the dc switch, and thus large on/off impedance ratios.

The scanning electron micrographs shown in Figures 7-1 and 7-2 reveal some of the key design innovations. The fabrication process allows the formation of corrugations in the cantilever, which are used to adjust the stiffness of the cantilever arm and contact region. The thickness of the release layer provides a step change in height in the cantilever arm next to the attachment area, which can be adjusted to tailor the actuation voltage. Corrugations have been incorporated in the cantilever arm where it attaches to the substrate to provide strain relief. Platinum is used for both contacts in the dc switch, and the process also

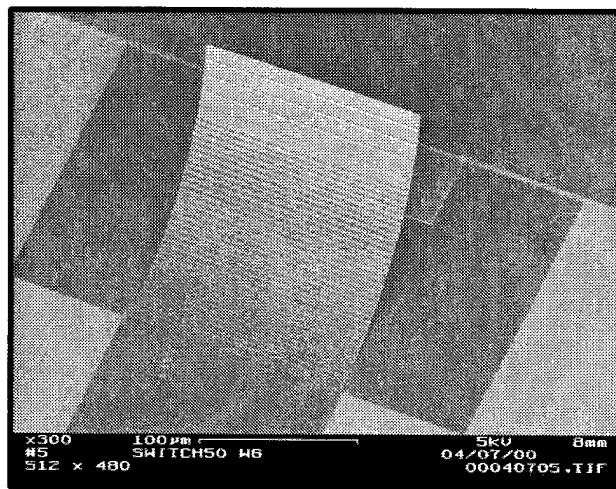
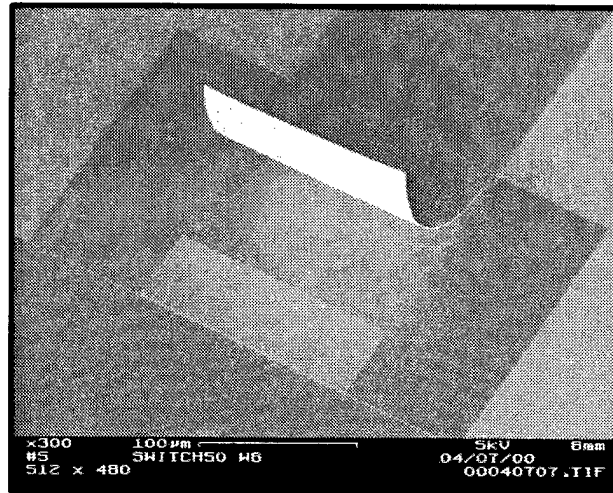


Figure 7-1. Two scanning electron micrograph (SEM) views of single capacitive microswitch. The moving capacitor plate can be seen at the end of the curved cantilever.

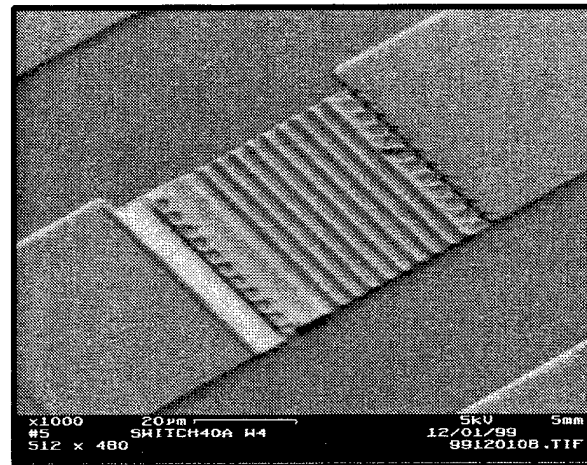
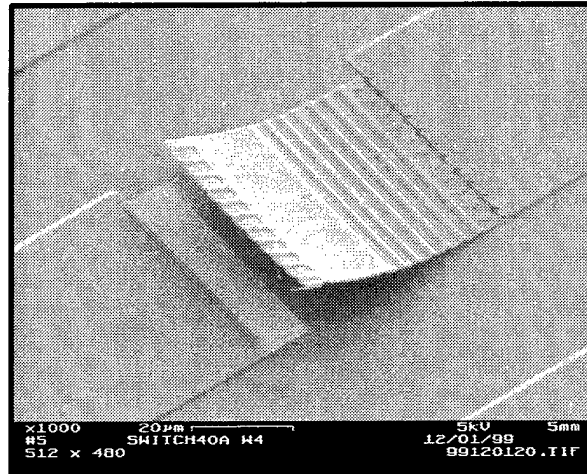


Figure 7-2. SEM photos of the dc contact microswitch open (top) and closed (bottom) states. The corrugations that are added for mechanical stiffness, and the contact dimples can be seen in the cantilever.

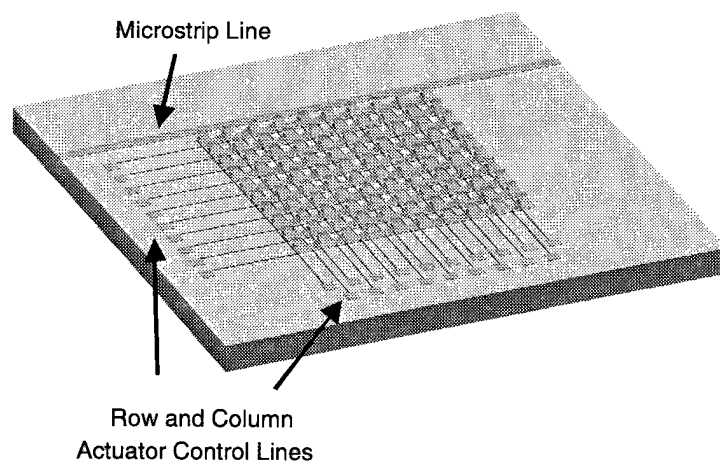


Figure 7-3. Conceptual diagram of two-dimensional microswitch array.

permits modifying the details of the contact region so that a variety of sizes and densities of contact points can be investigated. In the measurements given here, devices had ten contact dimples, each $2\text{ }\mu\text{m}$ in diameter, along the edge of the $50\text{-}\mu\text{m}$ -wide cantilever.

To facilitate rf measurements single switches were fabricated in a $50\text{-}\Omega$ coplanar waveguide circuit on a high-resistivity silicon substrate. The switches were placed across a gap in the center conductor and measurements were made using coplanar probes. Results from a capacitive contact version of the switch are shown in Figure 7-4. The closing time was measured to be $3\text{ }\mu\text{s}$, the opening time $20\text{ }\mu\text{s}$. The device successfully switched 2 W of microwave power at 10 GHz . The on-to-off impedance ratio was 200:1.

The dc switch measurements are shown in Figure 7-5. The switch in this figure had a contact resistance of $8\text{ }\Omega$, while other switches had considerably lower resistance. The initial yield measurements for these early results were 90% with $<10\text{ }\Omega$ and 30% with $<1.5\text{ }\Omega$. The switching speed for both the opening and closing was $<1\text{ }\mu\text{s}$.

C. Bozler	R. Drangmeister
S. Duffy	M. Gouker
J. Knecht	L. Kushner
R. Parr	S. Rabe
L. Travis	P. W. Wyatt
C. L. Keast	

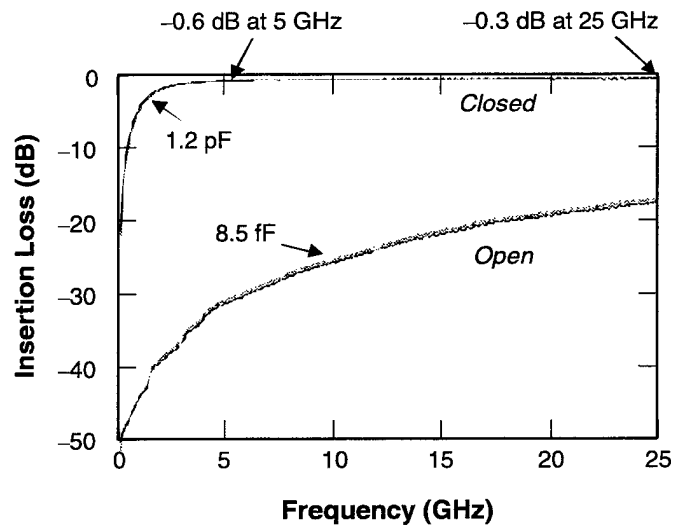


Figure 7-4. Measurement of capacitive switch characteristics. Each curve is a superposition of the measurement of five devices.

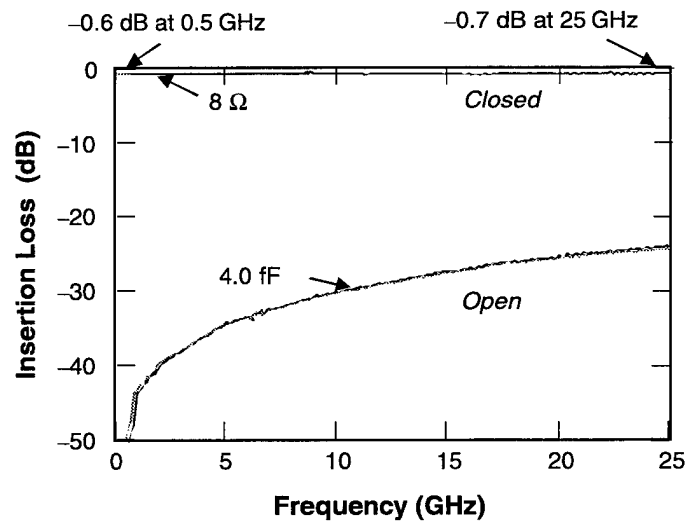


Figure 7-5. Measurements of dc switch characteristics. Each curve is a superposition of the measurement of three devices.

REFERENCE

1. Solid State Research Report, Lincoln Laboratory, MIT, 1996:3, p. 35.

